

# Properties of the Nili Fossae Olivine-phyllsilicate-carbonate lithology: orbital and in situ at Séítah

Adrian J. Brown<sup>\*1</sup>, Linda Kah<sup>2</sup>, Lucia Mandon<sup>3</sup>, Roger Wiens<sup>4</sup>, Patrick Pinet<sup>5</sup>, Elise Clavé<sup>6</sup>, Stéphane Le Mouélic<sup>7</sup>, Arya Udry<sup>8</sup>, Patrick J. Gasda<sup>9</sup>, Clément Royer<sup>10</sup>, Keyron Hickman-Lewis<sup>11</sup>, Agnes Cousin<sup>12</sup>, Justin I. Simon<sup>13</sup>, Jade Comellas<sup>14</sup>, Edward Cloutis<sup>15</sup>, Thierry Fouchet<sup>16</sup>, Alberto G. Fairén<sup>17</sup>, Stephanie Connell<sup>15</sup>, David Flannery<sup>18</sup>, Briony Horgan<sup>4</sup>, Lisa Mayhew<sup>19</sup>, Allan Treiman<sup>20</sup>, Jorge I. Núñez<sup>21</sup>, Brittan Wogsland<sup>2</sup>, Karim Benzerara<sup>22</sup>, Hans E.F. Amundsen<sup>23</sup>, Cathy Quantin-Nataf<sup>25</sup>, Kevin P. Hand<sup>26</sup>, Vinciane Debaille<sup>27</sup>, Ari Essunfeld<sup>9</sup>, Pierre Beck<sup>28</sup>, Nicholas J. Tosca<sup>29</sup>, Juan M. Madariaga<sup>30</sup>, Eleni Ravanis<sup>31</sup>, and Olivier Forni<sup>12</sup>

<sup>1</sup>Plancius Research, Severna Park, MD 21146. <sup>2</sup>Department of Earth and Planetary Sciences, University of Tennessee, Knoxville TN 37996, <sup>3</sup>LESIA, Observatoire de Paris, Université PSL, CNRS, Sorbonne Université, Université de Paris, Meudon, France, <sup>4</sup>Earth, Atmospheric, and Planetary Sciences, Purdue University, <sup>5</sup>IRAP, Observatoire Midi-Pyrénées, CNRS, Toulouse university, France, <sup>6</sup>CELIA, Université de Bordeaux, CNRS, CEA, <sup>7</sup>Laboratoire Planétologie et Géosciences, CNRS UMR 6112, Nantes Université, Université Angers, 44322 Nantes, France, <sup>8</sup>Department of Geoscience, University of Nevada Las Vegas, 89154 Las Vegas, NV, <sup>9</sup>Los Alamos National Laboratory, PO Box 1663 Los Alamos, NM 87545, <sup>10</sup>LESIA, Observatoire de Paris, Université PSL, CNRS, Sorbonne Université, Université de Paris, Meudon, France, <sup>11</sup>The Natural History Museum, Cromwell Road, London, SW7 5BD, UK, <sup>12</sup>IRAP, Observatoire Midi-Pyrénées, CNRS, Toulouse university, France, <sup>13</sup>Center for Isotope Cosmochemistry and Geochronology, Astromaterials Research & Exploration Science Division, NASA Johnson Space Center, 2101 Nasa Parkway, Houston, TX, 77058 USA, <sup>14</sup>University of Hawai'i at Mānoa, <sup>15</sup>University of Winnipeg, Canada, <sup>16</sup>LESIA, Observatoire de Paris, Université PSL, CNRS, Sorbonne Université, Université de Paris, Meudon, France, <sup>17</sup>Centro de Astrobiología (CSIC-INTA) & Cornell University, NY, <sup>18</sup>Queensland University of Technology, Queensland, Australia, <sup>19</sup>Department of Geological Sciences, University of Colorado Boulder, Boulder, CO 80309, <sup>20</sup>Lunar and Planetary Institute, Houston TX 77058, <sup>21</sup>Johns Hopkins University Applied Physics Laboratory, Laurel, MD 20723, <sup>22</sup>Institut de Minéralogie, Physique des Matériaux et Cosmochimie, CNRS, Museum National d'Histoire Naturelle, Sorbonne Université, Paris, France, <sup>23</sup>CENSSS, University of Oslo, Norway, <sup>25</sup>University of Lyon, France, <sup>26</sup>Jet Propulsion Laboratory, Pasadena, CA 91109, <sup>27</sup>Laboratoire G-Time, Université libre de Bruxelles, Brussels, Belgium, <sup>28</sup>Institut de Planétologie et d'Astrophysique de Grenoble IPAG/CNRS, Université Grenoble Alpes, 414 rue de la piscine, 38041 Grenoble cedex 09, France, <sup>29</sup>Department of Earth Sciences, University of Cambridge, Downing Street, Cambridge, CB2 3EQ, United Kingdom, <sup>30</sup>Department of Analytical Chemistry, University of the Basque Country UPV/EHU, 48940 Leioa, Spain, <sup>31</sup>Hawai'i Institute of Geophysics and Planetology, University of Hawai'i at Mānoa, Honolulu, HI, USA

Corresponding author: Adrian J. Brown ([adrian.j.brown@nasa.gov](mailto:adrian.j.brown@nasa.gov))

## 43 Key Points:

44

- 45 ● We use CRISM data and a Venn diagram analysis to show the Nili Fossae olivine  
46 lithology is better named olivine-phylllosilicate-carbonate
- 47 ● We postulate a flood lava origin for the olivine-phylllosilicate-carbonate at Séítah  
48 based on finding olivine cumulate with low viscosity
- 49 ● We find the phyllosilicate in the cumulate olivine at Séítah is likely talc, serpentine,  
50 hectorite, Fe/Mg smectite, saponite or stevensite

51

## 52 Plain Language Summary

53 We used orbital and in situ data to observe a lava flow containing the mineral olivine near the  
54 Mars 2020 landing site at Jezero Crater. By analyzing the reflectance spectra of the rocks  
55 containing the lava, we have identified that clay is present in the olivine bearing rocks. We use in  
56 situ imaging data to determine that the lava contains the olivine in close packed crystals  
57 (cumulate), a process which can happen in the bottom of a lake of lava. We use measurements  
58 from the SuperCam instrument to determine that the cumulate is accompanied by clays.

59

60

61

62

63

64

65 **Abstract**

66 We have studied the observed properties of the Nili Fossae olivine-phylllosilicate-  
67 carbonate lithology from orbital data and in situ by the Mars 2020 rover at the  
68 Séítah unit in Jezero crater, including: 1) composition 2) grain size 3) inferred  
69 viscosity (calculated based on geochemistry collected by SuperCam (Wiens et al.,  
70 2022)). Based on the low viscosity and distribution of the unit we postulate a flood  
71 lava origin for the olivine-phylllosilicate-carbonate at Séítah.

72 We include a new CRISM map of the phyllosilicate 2.38  $\mu\text{m}$  band and use in situ  
73 data from Mars 2020 SuperCam Laser Induced Breakdown Spectroscopy (LIBS)  
74 and VISIR and MastCam-Z observations to show that the phyllosilicate in the  
75 olivine cumulate in the Séítah formation is either talc, serpentine, hectorite, Fe/Mg  
76 smectite, saponite or stevensite.

77 We discuss two intertwining aspects of the history of the lithology: 1) the  
78 emplacement and properties of the cumulate layer within a lava lake, based on  
79 terrestrial analogs in the Pilbara, Western Australia, and using previously published  
80 models of flood lavas and lava lakes, and 2) the limited extent of post emplacement  
81 alteration, including phyllosilicate and carbonate alteration.

82

83

84

# 1. Introduction

## 1.1 Purpose of paper

This paper uses the latest findings of the Mars 2020 rover mission to infer the properties of the Nili Fossae olivine-carbonate lithology, including composition (Liu et al., 2022 and Corpolongo et al., this issue) and grain size (Tice et al., 2022), and uses this to calculate magma viscosity, based on the geochemistry of Wiens et al., (2022). We also use orbital CRISM data alongside in situ SuperCam reflectance measurements to derive new knowledge regarding the accompanying phyllosilicates in the olivine-carbonate lithology.

*Importance of Viscosity.* As we shall discuss further in this paper, the viscosity is a key characteristic of a lava flow, determined by a variety of factors, including its composition, temperature, water, crystal content and pressure. The viscosity is a critical parameter for controlling the morphologic expression of the erupted unit. Critically, it allows us to compare the lava with other similar flows across Mars, and place it in context with the dominant rock-forming processes on the planet. The inferred viscosity has now become available from the first in situ measurements of Jezero crater floor geochemistry.

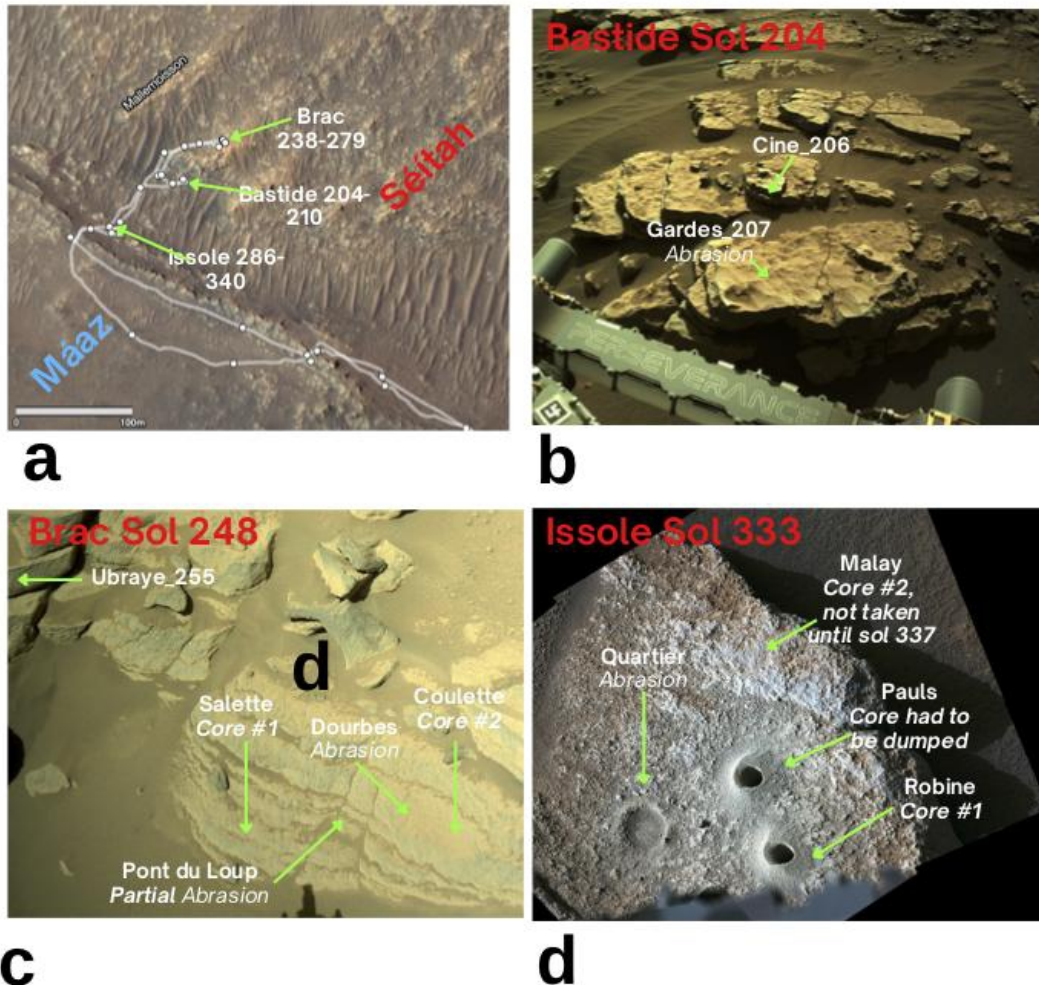
*Olivine-phyllosilicate-carbonate lithology and relationship to Landing Site.* The olivine-phyllosilicate-carbonate lithology was discovered using the Thermal Emission Spectrometer on the MGS spacecraft (Hoefen et al., 2003). It was subsequently mapped to extend throughout the Nili Fossae region, a region of radial graben on the northwest side of the Isidis Basin (Kremer et al., 2019). The landing site of the Mars 2020 rover was chosen to be at Jezero Crater, the site of a delta deposit which indicated the crater previously was filled with liquid water. The rover landed on Feb 18, 2021, sol 0 of the mission, to the south east of the delta (Sun et al., this issue). Around 200 sols (Martian days) later, the rover traversed around the edge of the Séítah region (Figure 1a), which is covered in linear dunes that were deemed to be too difficult to traverse. The dunes were determined from orbit to have a similar spectral signature to the olivine lithology mapped outside the crater (Godge et al., 2015).

Previously the lithology has been known to be olivine-bearing (Hoefen et al., 2003; Tornabene et al., 2008) or olivine-carbonate (Ehlmann et al., 2008; Mandon et al., 2020; Brown et al., 2020), however, this paper is designed to quantitatively analyze the relationship between olivine, carbonate and phyllosilicate and investigate, using a Venn diagrammatic approach; the suggestion that where there is carbonate, there is also clay (Horgan et al., 2020; Tarnas et al., 2021).

122 We address in detail two aspects of the olivine-phylllosilicate-carbonate lithologic  
 123 history: 1.) the emplacement of the cumulate layer within a lava lake, which is part  
 124 of a flood lava, based on terrestrial analogs in the Pilbara, Western Australia, and  
 125 previously published models of flood lava eruption and flow, and lava ponding in  
 126 lakes (Worster et al., 1993), and 2.) the limited extent of post emplacement  
 127 alteration, including phyllosilicate and carbonate alteration of the Séítah formation  
 128 (Clave et al., this issue; Mandon et al., this issue). These aspects of the history of  
 129 the unit demonstrate that observations and models are both needed to uncover  
 130 further insights into the emplacement and subsequent alteration history of this  
 131 important Martian lithology, which has now been sampled for return to Earth  
 132 (Simon et al., this issue).

133 *Unit Interpretations.* Farley et al. (2022) list definitions for the rock lithologies  
 134 discussed in this paper. Farley et al. defined the Séítah (an olivine cumulate) and  
 135 Mááz (a pyroxene- and plagioclase-dominated unit overlying Séítah) formations  
 136 that were encountered and mapped during the Crater Floor campaign in the first  
 137 380 sols of the Mars 2020 mission. We discuss interpretations arising from the  
 138 Séítah formation, which has previously been interpreted as related to the olivine-  
 139 carbonate lithology inside and outside Jezero. Figure 1 presents a visual summary  
 140 of the traverse through the Séítah formation and the three key workspaces, and all  
 141 the targets referred to in this paper. On Sol 202 of the mission the rover rolled into  
 142 the Séítah formation, and approached the Bastide workspace. For the purposes of  
 143 this study, the rover visited three main workspaces - in temporal order, Bastide,  
 144 Brac and Issole. These workspaces and the abrasions and samples taken at each  
 145 workspace are also shown in Figure 1. The rover left Séítah on Sol 340. See also  
 146 (Sun et al., this issue; Crumpler et al., this issue; Núñez et al., this issue) for more  
 147 details on the Crater Floor campaign and stratigraphic information obtained during  
 148 the Séítah traverse.





149

150 Figure 1. a.) HiRISE overview map of the Séítah traverse showing the three key workspaces: Bastide,  
 151 Brac, and Issole, and the Sol counts at each. b.) Navcam image of Bastide Workspace taken on Sol 204.  
 152 c.) Navcam image of Brac Workspace on Sol 248, before samples were taken d.) Mastcam-Z image of  
 153 Issole on Sol 333 after Robine and Pauls samples and Quartier abrasion were taken but before sample  
 154 Malay was obtained.

155 *Definition of phyllosilicate.* Due to its importance in this paper, we first establish a  
 156 clear and distinct definition of the word “phyllosilicate”. Here by “phyllosilicate”  
 157 we are referring to the mineral group of phyllo-silicates (“φύλλο” in Greek is  
 158 “leaf” in English). These layer-silicates have stacked hydroxyl (-OH), octahedral  
 159 (O) sheets and tetrahedral (T) silicate (Bailey, 1988). The octahedral sheets come  
 160 in two forms called dioctahedral and trioctahedral which host divalent ( $\text{Fe}^{2+}/\text{Mg}^{2+}$ )  
 161 and trivalent (e.g.,  $\text{Al}^{3+}/\text{Fe}^{3+}$ ) cations respectively. Phyllosilicates come in many  
 162 families, based on the stacking of layers (e.g. TO or 1:1 vs TOTTOT or 2:1). In this  
 163 paper we are particularly interested in the 2:1 phyllosilicates talc and 1:1  
 164 serpentine and the 2:1 phyllosilicate family called smectites.

## 1.2 Previous work

### 1.2.1 Infrared remote observations

The Syrtis Major shield region was first observed to host olivine using Visible and Near InfraRed (VNIR) telescopic observations by Pinet and Chevrel (1990). Spacecraft observations followed, and a decade later the Thermal Emission Spectrometer (TES) infrared (IR) instrument also recognised a strong 10  $\mu\text{m}$  absorption band associated with the Nili Fossae region that was attributed to olivine (Hoefen et al., 2003). The Observatoire pour la Minéralogie, l'Eau, le Glace et l'Activité (OMEGA) instrument on Mars Express was able to determine that phyllosilicates were also associated with the olivine, suggesting Fe-rich smectites were present (Mangold et al., 2007). Using data from the Compact Reconnaissance Imaging Spectrometer for Mars (CRISM) instrument, Mg-carbonate was discovered to be associated with the olivine lithology by using the strength and position of the 2.5  $\mu\text{m}$  band (Ehlmann et al., 2008). The olivine-carbonate was hypothesized to be due to serpentinization by Brown et al. (2010), who also suggested that talc might be present by analogy to talc-carbonate terrestrial Archean greenstone terranes. Brown et al. (2010) also found the carbonate to be a 50/50 Fe/Mg mixture, which was later supported using TES orbital data analyzed by Ruff et al. (2022). Goudge et al. (2015) mapped the watershed of the Jezero deltas and the accompanying mineralogy. Mafic minerals and marginal carbonates were identified in the mapping of Horgan et al. (2020). Mandon et al. (2020) used OMEGA observations to map the olivine and carbonate, and used crater counting to date the unit at 3.82 Ga. The olivine composition (Fo#44-66) and grain size ( $\sim 1\text{mm}$ ) were calculated by Brown et al. (2020) using CRISM data.

A recent map of the mineralogy of Jezero crater using CRISM data illustrates the locations of multiple minerals and mineral combinations including olivine, Mg-rich carbonate, olivine+Fe/Mg-smectite, high-Ca pyroxene, and low-Ca pyroxene (Parente et al., 2021). This map was created using a new algorithm for atmospheric correction (Itoh and Parente, 2021) that enhances the spectral features due to surface outcrops and an improved mapping procedure (Saranthan and Parente, 2021).

Finally, a recent closely related study of VNIR spectra of phyllosilicates in the Archean Barberton Greenstone Belt has identified serpentine and chlorite after olivine and suggested that the phyllosilicates were formed by hydrothermal alteration (Grosch et al., 2021).

### 202 1.2.2 SuperCam LIBS observations

203 SuperCam is a multi-technique instrument suite mounted on the Mars 2020  
 204 *Perseverance* rover (Wiens et al., 2021; Maurice et al., 2021). It is an upgraded  
 205 version of the ChemCam instrument onboard the Mars Science Laboratory (MSL)  
 206 *Curiosity* rover. It has the capability to obtain LIBS measurements to a distance of  
 207 ~10 m, and to quantify the major element abundances at distances up to 6.5 m. The  
 208 Remote Micro-Imager (RMI) is a color telescope used to provide context images  
 209 for SuperCam observations.

210 The SuperCam instrument has been used to investigate the igneous nature of the  
 211 Séítah and Máaz regions, as reported by Wiens et al. (2022). That study  
 212 concentrated on chemistry and mineralogy, and creation of a stratigraphy of the  
 213 two regions of the Jezero crater floor. In this paper we use LIBS elemental  
 214 abundances for the Séítah and Máaz formations reported in the Wiens et al. (2022)  
 215 study.

### 216 1.2.3 SuperCam VISIR observations

217 SuperCam VISIR is an optical spectrometer that covers the 0.4-0.85 and 1.3-2.6  
 218  $\mu\text{m}$  wavelength ranges, providing reflectance spectra boresighted with LIBS and  
 219 RMI instruments (Fouchet et al., 2022). This paper relies on the calibration and  
 220 comparison of the spectra presented here with others measured on the surface.  
 221 Royer et al. (this issue) shows that, based on band depth calculations and noise  
 222 estimates, that most of the 2.46  $\mu\text{m}$  detections we will discuss herein range from  
 223 Signal to Noise Ratio (SNR) = 4 to SNR = 12. This spectral range is harder to  
 224 study because of the fact that many spectral signatures are sampled with the  
 225 minimum sampling (at most 2 spectral channels in the band) and several artifacts  
 226 may be similar to absorption features (e.g., non-corrected spikes, calibration  
 227 residuals). In our case, regarding the 2.46  $\mu\text{m}$  region, we have SNR > 5 and as  
 228 demonstrated below, detections of small bands in this region are realistic, given the  
 229 accuracy of the calibration and the potential residuals. Positive detections must  
 230 nevertheless be confirmed visually and their attribution validated by the presence  
 231 of other features characteristic of phyllosilicates.

232 SuperCam's VISIR data allow on-ground comparison with absorption features seen  
 233 from orbit by the CRISM instrument. Due to the fact that CRISM covers a larger  
 234 spectral range (0.4-3.96  $\mu\text{m}$ ), in this paper we adopt a band fitting strategy over the  
 235 1.3 to 2.5  $\mu\text{m}$  range.

236



#### 237 *1.2.4 PIXL observations*

238 PIXL is a high resolution X-Ray fluorescence microscope in situ scanning  
 239 instrument mounted on the arm turret of the rover (Allwood et al., 2020). PIXL  
 240 observations of the Dourbes target have been used to identify the cumulate nature  
 241 of the target and infer an igneous origin (Liu et al., 2022). The olivine composition  
 242 is consistently homogeneous, and of Fo55+/-1 within a several mm analysis patch  
 243 (Liu et al., 2022), which is a remarkable match with previous orbital work  
 244 constraining the olivine Fo# to 44-66 (Brown et al., 2020). PIXL's X-ray  
 245 diffraction capability, which can identify coherent crystalline domains, has been  
 246 used to identify coarsely grained (1-2 mm), interlocking olivine grains (Tice et al.,  
 247 2022), and SuperCam's RMI instrument measured a mean grain size of 1.45+/-0.20  
 248 mm over the rover's Seitah formation traverse (Wiens et al. 2022). These in situ  
 249 observations are both good matches for the ~1 mm Nili Fossae olivine grain size  
 250 calculation from orbital studies prior to landing (Brown et al., 2020).

251

## 252 **2. Methods**

253

### 254 *2.1 Viscosity calculations*

255

#### 256 *2.1.1 Bottinga and Weill empirical melt viscosity model*

257

258 In order to calculate the inferred melt viscosity, we have used the empirical  
 259 approach of Bottinga and Weill (1972), which calculates a viscosity vs.  
 260 temperature curve for the magmatic silicate liquid. Their method uses five look-up  
 261 tables according to the silica content of the magma. They then use these tables to  
 262 sum the contributions of the elements common to terrestrial magma bodies to  
 263 arrive at a inferred viscosity for a magma of that composition.

264

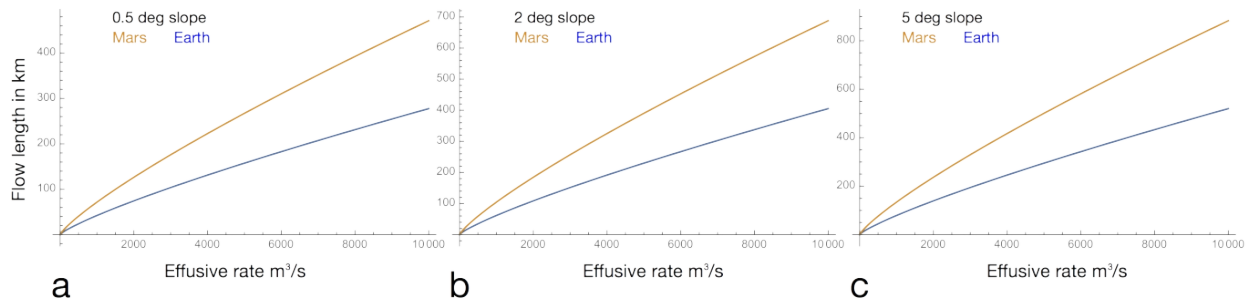
265 We have used the SuperCam LIBS geochemical elemental abundances for the  
 266 Máaz formation, Artuby member and Séítah formation from Wiens et al. (2022).  
 267 Wiens et al. (2022) made a partial correction for the LIBS compositions by  
 268 removing all data points that were float rocks, soils, and apparent coatings, as well  
 269 as all points that had major-element totals < 80 wt%. The latter step removes a  
 270 large number of points with alteration, especially anything that included significant  
 271 sulfate or carbonate contributions. Wiens et al. (2022) investigated how the  
 272 removal of points affected the bulk compositions, and determined that the 80 wt%  
 273 was a reasonable limit. In this study, we have made no further attempt to  
 274 petrologically correct the measured bulk compositions to the original magma, and

will instead pursue this approach in future work.

276

### 277 2.1.2 Flood lava and lava lake models

278 Martian gravity is ~37.5 % of that on Earth. Assuming Mars possessed a thinner  
 279 (~6 mbar) atmosphere throughout its history, we can compare terrestrial lava  
 280 properties to those of Mars (Wilson and Head, 1994). On Mars, with a thinner  
 281 atmosphere, lava will take longer to cool. Longer cooling rates should also drive  
 282 larger crystal growth. Wilson and Head (1994) predicted Martian volcanic flows  
 283 (driven by lower gravity) to be 6 times as long as compositionally identical flows  
 284 on Earth, leading to spatially larger deposits on the smaller planet.



286 Figure 2. Lava flow lengths for Martian and Earth conditions for three different ground slopes. Modeled  
 287 after Wilson and Head (1994), and recalculated using eqn (1). Angles are in degrees.  
 288

289 Pinkerton and Wilson (1994) presented a Bingham non-isothermal model for  
 290 calculation of the runout lengths for lavas on Earth. This model depends upon  
 291 viscosity, so we used this equation to calculate the expected runout length  $L$  in  
 292 Figure 2 for Mars and Earth gravity. This is Equation 7 of Wilson and Head (1994):  
 293

$$294 \quad L = [1.34/\kappa G_{zc}](\tau/\eta)^{2/11} E^{9/11} [\tau/(\rho g)]^{6/11} \sin^{3/11} \alpha \quad (1)$$

295

296 where  $\kappa$  is the thermal diffusivity of lava, taken as  $7 \times 10^{-7} \text{ m}^2/\text{s}$ ,  $G_{zc}$  is the critical  
 297 Grätz number, taken as 300,  $\tau$  is the yield strength of the lava, taken as 2000 Pa,  $\eta$   
 298 is the plastic viscosity,  $(\tau/\eta)^{2/11}$  is taken as 0.38 as suggested by Wilson and Head  
 299 (1994),  $\rho$  is the density of the lava, taken here as a value appropriate for ultramafic  
 300 lavas of  $3200 \text{ kg/m}^3$ ,  $g$  is the acceleration due to gravity,  $9.81 \text{ m/s}^2$  for Earth and  
 301  $3.72 \text{ m/s}^2$  for Mars,  $\alpha$  is the average slope angle in degrees of the ground over  
 302 which the lava flows. The results of this calculation are shown in Figure 2. Note  
 303 that our values are a factor of 10 less than Figure 8b of Wilson and Head (which  
 304 suggests flow lengths of up to 7000km, however only discusses flows up to 700km  
 305 in the text of the paper) These show that run out flows of 300 to 700 km are

possible with the highest effusion rates, and that Martian flows are roughly 1.7 times as long as their terrestrial duals under the Pinkerton-Wilson model. In addition to this, a 5 times higher effusion rates is expected on Mars due to two fold greater dike widths expected due to lower gravity. These two factors lead to the factor of 6 times flow lengths expected on Mars. Martian lavas of length around 600km (such as Syrtis Major) would be equivalent to a 100km diameter lava on Earth (similar to the exposed current extent of the Warrawoona Group basalts in the Pilbara region (Van Kranendonk et al. 2002)).

In addition, the Pinkerton and Wilson model actually uses an implicitly high viscosity due to the  $(\tau/\eta)^{2/11} = 0.38$  and  $\tau = 2000$  we get  $\eta \sim 409468$ . For lower plastic viscosities we derive in this paper, the model predicts greater run out lengths are possible.

Finally, it should be noted that the Pinkerton and Wilson (1994) model is appropriate only in the case of “cooling-limited” flows, where the lava flow halts as it cools (Guest et al., 1987). If the lava flow is halted due to a magma cut off, the flow will be “volume-limited” and much shorter than calculated using equation (1).

The Reynolds number of a liquid flow can be calculated as (Huppert et al., 1984):

$$R_e = E/\nu \quad (2)$$

Here  $E$  is the discharge rate and  $\nu$  is the kinematic viscosity.  $R_e$  is a threshold for turbulence, the critical value is typically  $\sim 2000$ .

At high Reynolds number, the discharge rate  $E$  of lava through a long fissure of width  $d$  can be calculated thus:

$$E = d^{3/2}(g\Delta\rho)^{1/2}/(k\rho)^{1/2} \quad (3)$$

Here  $k$  is a friction coefficient,  $\Delta\rho$  is the density difference between the magma and lithosphere, and  $\rho$  is the magma density. On Mars, as mentioned earlier, wider fissures  $d$  are expected by a factor of two, and this outweighs weak (square root) dependence on gravity, for otherwise identical flows, discharge rates will be 6 times than on Earth.

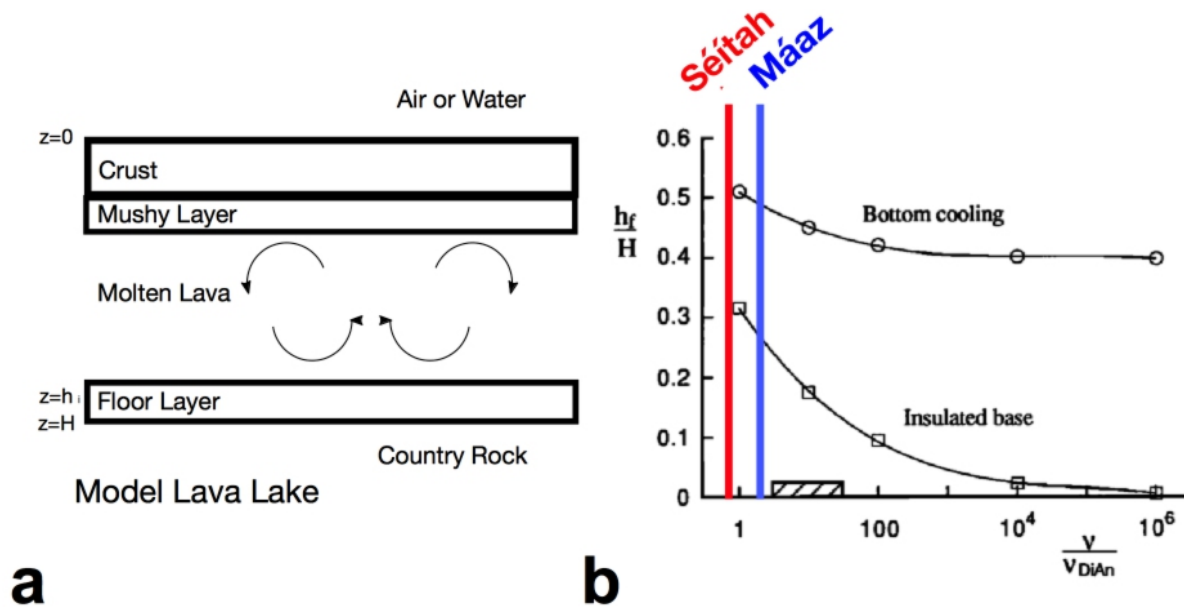


Figure 3. a.) Thermal model of a lava lake with layers representing solid crust/cap, mushy layer (where crystals form), molten lava (with convection taking place) and the floor. b.) Final fractional height of floor layer,  $h_f$ , where crystals accumulate (relative to the height of the chamber height,  $H$ ) plotted against the lava viscosity (normalized relative to liquid diopside). Two cases are shown, one in which bottom cooling occurs, and one in which it does not (insulated base). The dashed box indicates the viscosity of typical terrestrial basalt relative to a pure diopside melt, after Worster et al. (1993). The Séitah and Máaz viscosities calculated in this paper are schematically shown on the plot.

*Development of layering.* The large grain size (Tice et al., 2022) and cumulate texture (Liu et al., 2022; Tice et al., 2022) lead us to explore the possibility of the Séitah rocks being emplaced as a Martian lava lake. Worster et al. (1993) developed a thermodynamic model for a terrestrial lava lake, and outlined how the body would form compositional and textural layers within the resultant rock as it cooled. They showed that a lava lake can develop quickly when a magma body is exposed to the atmosphere, and showed that convective cooling can take place. They examined the situation with and without convection in their model and found thermal convection drives internal crystallization within the melt. This in turn forms layering within the floor of the lake. Cooling by thermal conduction alone does not produce this layering. Figure 3a shows a schematic diagram of an idealized lava lake after Worster et al. (1993). For our purposes, we will define a lava lake as a connected igneous body that is cooling convectively and develops internal stratification (i.e. layering) as shown in this diagram.

*Effect of viscosity.* Figure 3b shows the effect of viscosity on the cooling history of

a lava lake that is cooled from the top. This figure shows the major effect of viscosity on lava lake crystallization, as studied by Worster et al. (1993). The parameter  $h_f$  is the final floor layer (Figure 3a) depth, and  $H$  is the total depth of the lava lake. It can be seen that the relative size of the floor layer grows with decreasing viscosity, and this effect is more pronounced when the bottom of the rock is insulated. We show schematically with vertical lines where the Séítah and Máaz units viscosity would plot (relative to liquid diopside), indicating that Séítah-like viscosities would produce a deeper cumulate floor layer than a Máaz-like viscosity. The equation for the calculation of the viscosity of diopside adopted by Worster et al. (1993) (their Table 2) is:

$$\eta = \exp[12 - 52.5x + 62.5x^2] \ln(10) \quad (4)$$

where  $x = 1 - 1000/(T + 273)$  and  $T$  is the temperature of the melt in degrees C.

The takeaway message from this section is that lower viscosity lavas build thicker cumulate layers. We shall use this model to enhance the interpretations of our in situ observations later in this study.

## 2.2 *Phyllosilicate alteration mineralogy*

We will now discuss the methods used in this paper to analyse visible to near infrared (VNIR, 0.4-2.5  $\mu\text{m}$ ) reflectance spectra to identify and map phyllosilicates using asymmetric band fitting, and give a short introduction to the chemical formulas of the phyllosilicates that we are interested in for this study.

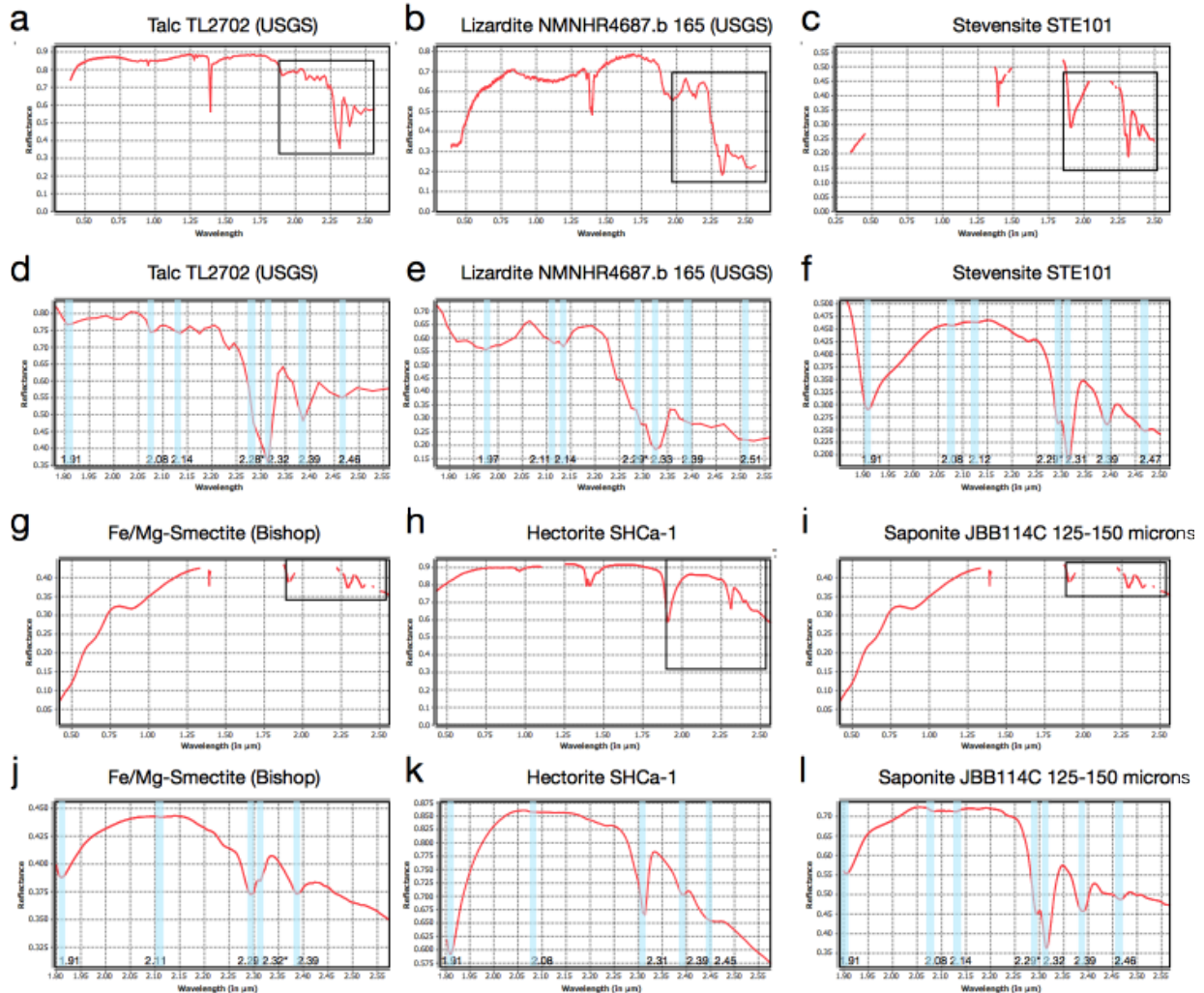
For this study we have used a single image cube of CRISM data from the Map Projected Targeted Data Record (MRTDR) calibration standard, as described by Seelos et al. (2012). This processing level removes all atmospheric effects and presents each pixel in apparent reflectance space, which is suitable for comparison with spectral library spectra or SuperCam VISIR processed spectra.

### 2.2.1 *CRISM and VISIR phyllosilicate identification*

Figure 4 shows library spectra of talc, lizardite, stevensite, Fe/Mg smectite, hectorite and saponite in the VIS and SWIR (Short Wave InfraRed) regions, which are covered by the SuperCam VISIR instrument. The talc and lizardite spectra are



413 sourced from the USGS Spectral Library (Clark et al 2007). The stevensite  
 414 specimen was provided by Nicholas Tosca and measured at the University of  
 415 Winnipeg Planetary Spectrophotometer Facility. The Fe/Mg smectite, hectorite and  
 416 saponite spectra were supplied by Janice Bishop. Information on the samples is  
 417 supplied in the supplementary section S2.  
 418



419 Figure 4. Laboratory spectra of a.,d.) Talc b.,e.) Lizardite c.,f.) Stevensite g.,j.) Fe/Mg-smectite (Bishop)  
 420 h.,k.) Hectorite SHCa-1, i.,l.) Saponite JBB114C. Shown at top is the visible and SWIR region of the  
 421 spectrum, on the bottom is a zoom into the SWIR region at the location shown in the box on the lower  
 422 spectra. Note: 1) strength of 2.31  $\mu\text{m}$  band in talc and 2) the presence of a weak 2.46  $\mu\text{m}$  band in talc  
 423 which is not present in lizardite.  
 424  
 425

426 The SWIR absorption bands of the Fe-bearing phyllosilicates nontronite (Bishop et  
 427 al., 2013) and hisingerite (Turrenne et al., this issue) both display strong 2.28  $\mu\text{m}$   
 428 bands which are not present in the spectra of olivine bearing targets we report here,

so they are not considered further.

The key bands of the spectra are noted in the plot, and we draw the reader's attention to the relative strength of the 2.31 (strong), 2.38 (moderate to weak) and 2.46  $\mu\text{m}$  (weak) bands in particular. The two key differences for the purpose of this paper are 1) the strength of the 2.38  $\mu\text{m}$  band, which is present in the serpentine lizardite (Figure 4e), but far stronger in talc (Figure 4d), and 2) the presence of a weak 2.46  $\mu\text{m}$  band in talc (Figure 4e) which is only a shoulder (at most) in lizardite (Figure 4e). These spectral differences will be discussed in the remainder of the paper.

#### *2.2.1.2 Band fitting with an Asymmetric Gaussian shape*

As has been previously discussed in a variety of forums such as Brown (2006), the natural bandshape for an absorption band in energy space is a Gaussian shape. When accompanied by nearby and often closely related bands, for example, due to Tschermak substitution of  $\text{Mg}^{2+}$  and  $\text{Fe}^{2+}$  (Duke, 1994), the vibration bands can adopt an asymmetric shape. It is then advantageous to carry out an asymmetric band fit. Figure 4 demonstrates that all three of the phyllosilicate related bands are asymmetric and extend to the left (higher energy). As part of this fitting process we obtain four parameters per band: the amplitude, width, centroid (position), and the asymmetry (Brown et al., 2010). We primarily use the amplitude band parameter, and cross-correlate the amplitude of the olivine 1  $\mu\text{m}$  band, 2.31  $\mu\text{m}$  (phyllosilicate or carbonates), 2.5  $\mu\text{m}$  (carbonate only), 2.38  $\mu\text{m}$  (phyllosilicate only) band amplitude maps.

#### *2.2.2 Ideal Chemical formulas of serpentine, talc and smectites*

*Smectites.* Dioctahedral smectites contain two cations with a charge of 3+ (typically  $\text{Al}^{3+}$  or  $\text{Fe}^{3+}$ ) in their octahedral sheets (for example montmorillonite and nontronite), while trioctahedral smectites contain three cations with a charge of 2+ (typically  $\text{Mg}^{2+}$  and sometimes  $\text{Fe}^{2+}$  or other transition metals) with the Mg-rich form called hectorite, stevensite, or saponite, where saponite has tetrahedral substitution and hectorite does not. Stevensite has additional charge due to cation vacancies in the octahedral sheets.

Beidelite and saponite are special cases of smectites where  $\text{Al}^{3+}$  substitutes for  $\text{Si}^{4+}$  in the tetrahedral sheets, causing a disruption of the structure and creating surface charge. Nontronite and hectorite do not typically contain any  $\text{Al}^{3+}$  cations. We note

that the Fe/Mg-smectite proposed to best match the spectral properties of the most common phyllosilicate on Mars is a smectite containing a mixture of both  $\text{Fe}^{2+}$  and  $\text{Mg}^{2+}$  cations, but no  $\text{Al}^{3+}$  cations, termed “Fe/Mg-smectite” (Bishop et al., 2008a,b).

Saponite is also frequently considered the subgroup name for trioctahedral smectites; under this definition there are “saponites” with no  $\text{Al}^{3+}$  cations that resemble hectorite and there are high Al-substitution saponites that have significant substitution of  $\text{Al}^{3+}$  for  $\text{Si}^{4+}$  in the tetrahedral sheets. As it is difficult to determine the degree of Al-substitution in saponites without detailed sample characterization, this mineral name can be confusing. This confusion is often compounded because saponite is much more common on Earth than hectorite, and thus lab samples of saponite are more readily available for study. However, Mg-rich smectites do not require  $\text{Al}^{3+}$  in their structures, for example, saponite has tetrahedral substitution whereas hectorite does not.

*Non-smectites.* The ideal chemical formula of lizardite (Mg-serpentine) is  $\text{Mg}_3\text{Si}_2\text{O}_5(\text{OH})_4$ , and that of Mg-talc is  $\text{Mg}_3\text{Si}_4\text{O}_{10}(\text{OH})_2$ . For the purposes of this study, we point out that there is no aluminum in their structure. In contrast, the Mg-chlorite, clinochlore has an ideal formula of  $(\text{Mg},\text{Fe}^{2+})_5\text{Al}(\text{Si}_3\text{Al})\text{O}_{10}(\text{OH})_8$ . A similar amount of  $\text{Al}^{3+}$  is present in micas such as the dioctahedral muscovite  $\text{KAl}_2(\text{AlSi}_3\text{O}_{10})(\text{F},\text{OH})_2$  and trioctahedral biotite  $\text{K}(\text{Mg},\text{Fe})_3\text{AlSi}_3\text{O}_{10}(\text{F},\text{OH})_2$ .

### 3. Results

#### 3.1 Viscosity results and lava lake calculations

Table 1 presents the elemental abundances derived using SuperCam LIBS measurements on rocks from the Máaz formation, Artuby member and Séítah formation. The LIBS data are obtained from Table 2 of Wiens et al. (2022). The elemental compositions are averages over many targets within the respective units. The CIPW norm mineral sum is slightly below 100 wt% because Wiens et al. assumed a small amount of apatite based on observations of phosphorous – Ca – F/Cl/H LIBS peak associations in a few targets; however, the P, Cl, F, and H abundances are not quantified, which leads to a small mass deficit.

The CIPW norms in Table 1 provide estimated igneous mineral content in the absence of alteration by carbonates or phyllosilicates. Wiens et al. (2022) removed observations that had clear evidence of alteration. In this paper, we will use this elemental abundance data to calculate the viscosity, and later we will discuss the

low Al content of the olivine bearing unit in the Séítah unit in relation to phyllosilicate identification.

The bottom line of the table shows the calculated viscosity at 1450 K. This calculation was conducted using the Bottinga-Weill empirical melt viscosity technique described earlier. The results of this calculation are plotted against the inverse temperature in Figure 5a. We have presented the viscosity results in this manner (“Arrhenius Plot” of natural log of viscosity versus the inverse temperature) because this is the format of the viscosity plots of Bottinga and Weill (for example their Figure 7). We then used equation (1) to calculate the length of the flow in the same way Figure 2 was calculated. We have used three different viscosities and two different gravities, and plotted the six lines in Figure 5b.

*Relative viscosity analysis.* As discussed in Section 2, viscosity has a large effect on the properties of lava lakes. We showed in Figure 3b the schematic relative viscosity values for the Máaz and Séítah formations relative to the viscosity of diopside. We are now in a position to justify this calculation. Using equation (4), we can calculate the model viscosity for diopside at 1450K as 382.54, and using the last line of Table 1, see that it lies between the viscosities at the same temperature of Séítah (88.55) and Máaz (472.68). We note that we are obliged in this comparison to estimate a temperature relevant for the lava lake model.

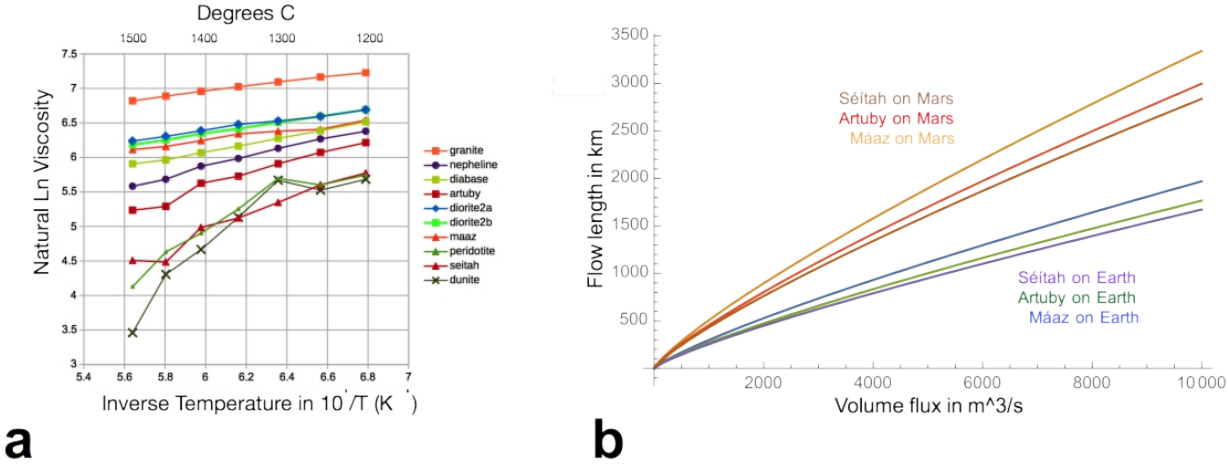
*Viscosity Error analysis.* In order to provide some measure of the error of these viscosity derivations, we use the error estimate from Anderson et al. (2022). The average Root Mean Squared Error of Prediction (RMSEP) from their Table 5 is 1.85 wt %. We also use the error estimate from Bottinga and Weill (1972) for their viscosity model. Figure 6 of Bottinga and Weill shows that 99% of their observations are within  $-0.75 < \Delta \ln \eta < 0.75$  of their viscosity model. We therefore use  $\pm 0.75$  as the error band for the  $\ln$  viscosity

Table 1. Elemental abundances and normative mineralogies obtained using SuperCam LIBS during the Crater Floor campaign (Wiens et al., 2022). All elemental data are in wt % and the CIPW norm abundances are in %.

Element oxide (wt %)	Máaz	Artuby	Séítah
SiO <sub>2</sub>	54.2	49.7	44.8
TiO <sub>2</sub>	0.6	0.9	0.2
Al <sub>2</sub> O <sub>3</sub>	10.5	7.4	3.9
FeO <sub>T</sub>	20.2	25.3	22.6
MgO	2.7	3.8	21.4

CaO	5.5	7.7	3.6
Na <sub>2</sub> O	3.3	2.7	1.3
K <sub>2</sub> O	1.2	0.6	0.2
Quartz	5.6	0.0	0.0
Plagioclase	37.9	30.0	15.2
Orthoclase	7.1	3.6	1.2
Diopside	4.8	16.7	1.5
Hypersthene	37.9	41.5	34.7
Olivine	0.0	0.9	41.1
Ilmenite	1.1	1.7	0.4
Magnetite	1.6	2.0	1.8
An # plag	25.3	22.7	26.5
Mg #	19.3	21.1	62.8
Density (g/cc)	3.10	3.27	3.37
	±0.02	±0.03	±0.01
Viscosity at 1450° K	472.68	18.37	88.55

540  
541  
542  
543  
544



546 Figure 5. a.) Arrhenius plot of natural log of viscosity versus inverse temperature calculations for Máaz,  
547 Artuby, and Séítah rocks compared with terrestrial samples, including granite, diorite and dunite.  
548 Viscosity error bars are +/- 0.75 and are the same for all points. b.) Flow lengths for viscosities of Séítah,  
549 Artuby and Máaz on Earth and Mars.

550  
551



## 3.2. Phyllosilicate alteration

### 3.2.1 CRISM orbital maps

To visualize the phyllosilicates that are present in the olivine-phyllosilicate-carbonate, we have produced a map of the orbital CRISM Half Resolution Long (HRL) image, HRL40FF, over Jezero crater (Figure 6). This includes the area of Mars 2020 operations, Octavia E. Butler Landing site, Jezero Delta, and the marginal carbonates region (Williford et al., 2018; Farley et al., 2020; Stack et al., 2020). Alongside a 0.905  $\mu\text{m}$  channel image, we have included three absorption band maps from the CRISM image for 2.31  $\mu\text{m}$  (phyllosilicate and carbonate), 2.5  $\mu\text{m}$  (carbonate) and 2.38  $\mu\text{m}$  (phyllosilicate). Here we focus on the phyllosilicate signature; for more discussion of the carbonate spectral signature, see (Mandon et al., 2020; Brown et al., 2020; Zastrow and Glotch, 2021).

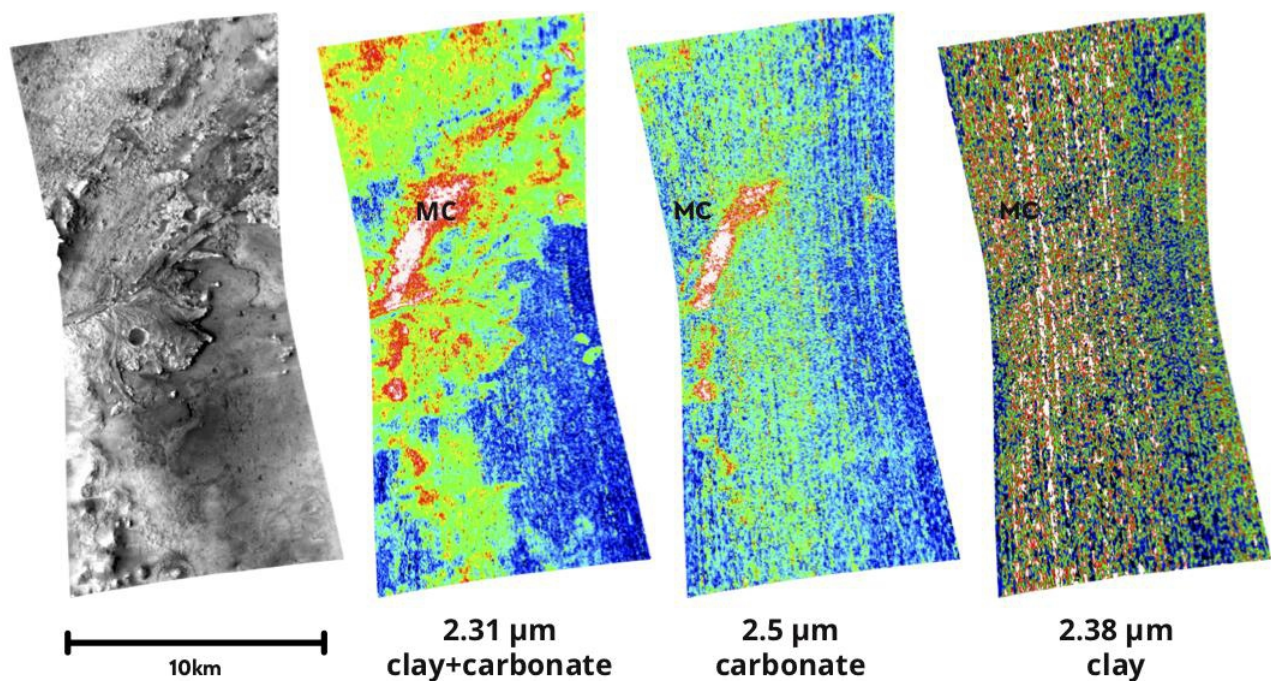
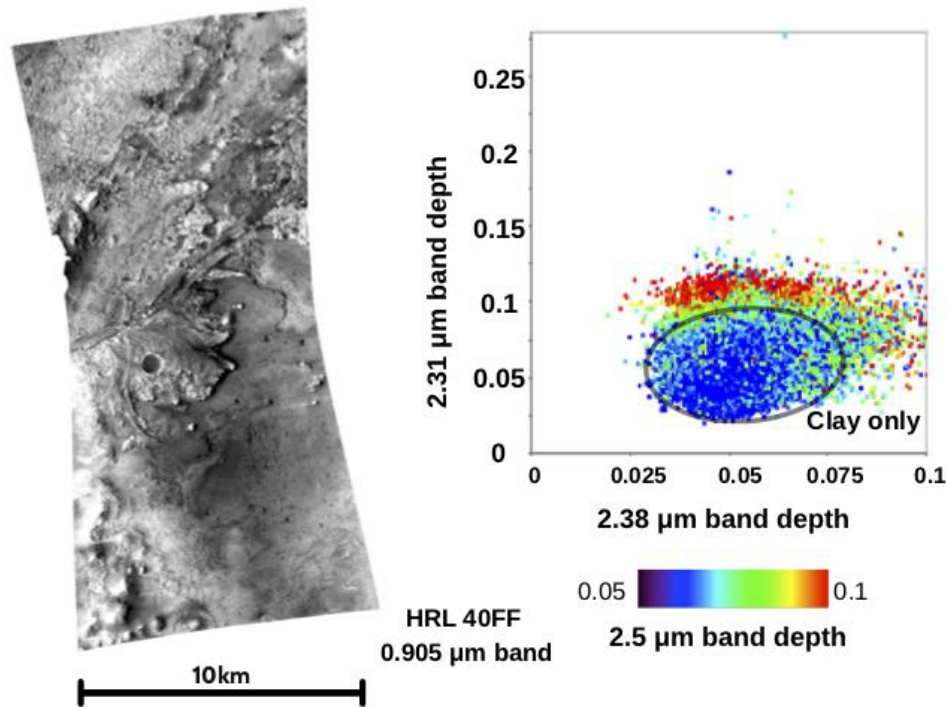


Figure 6. HRL40FF 0.905  $\mu\text{m}$  map, 2.31  $\mu\text{m}$ , 2.5  $\mu\text{m}$ , 2.38  $\mu\text{m}$  band amplitude maps. The location of the marginal carbonates is also shown as MC.

### 3.2.2 Correlation maps

As can be seen from Figure 6, mapping the 2.38  $\mu\text{m}$  phyllosilicate band is very difficult due to it being close to the noise level. To overcome this and gain further

insights into the presence of phyllosilicates in the CRISM HRL40FF image, we have constructed a correlation map consisting of the 2.31, 2.38 and 2.5  $\mu\text{m}$  bands. For each of these three band maps, we have the four parameters of the Asymmetric Gaussian band, meaning we have 12 parameters total. Figure 7 displays the correlation plots for HRL40FF for band depth amplitude (2.38)-amplitude(2.31)-amplitude(2.5). This can be interpreted as the  $x$  value being the amplitude of the 2.38  $\mu\text{m}$  band, the  $y$  value as the amplitude of the 2.31  $\mu\text{m}$  band, and the coloring of the points reflects the amplitude of the 2.5  $\mu\text{m}$  band.



583

Figure 7. HRL40FF correlation plots of the 2.38  $\mu\text{m}$  band depth ( $x$ -axis) vs. the 2.31  $\mu\text{m}$  band depth ( $y$ -axis). Color indicates the 2.5  $\mu\text{m}$  band depth, with red>green>blue.

586

These correlation plots show when all three bands are present and to what degree. Figure 7 shows that the points that are high in 2.5  $\mu\text{m}$  amplitude are also high in 2.31  $\mu\text{m}$  band amplitude. This allows us to be very specific and make a finding: there are regions of the HRL40FF image that display the presence of all three bands (known as the marginal carbonates, marked on Figure 6). However, there are regions where only phyllosilicates are present, with only a weak to vanishing 2.5  $\mu\text{m}$  carbonate band, indicated by blue colored points. This is marked “Phyllosilicate only” on the Figure 7 correlation plot. This plot makes clear that the highest 2.5  $\mu\text{m}$  band amplitudes are correlated with the highest 2.31  $\mu\text{m}$  band amplitudes.

597

### 3.2.3 Venn diagrammatic approach

To get a quantitative estimate of the phyllosilicate and carbonate present with the olivine in this image, we present a Venn diagram populated with data from HRL40FF where olivine, phyllosilicate and carbonate are determined to be present. In order to construct this diagram, we used the following detection rules for the olivine, carbonate, and phyllosilicate bands, which were arrived at iteratively to produce the least noisy CRISM maps, based on previous work (Brown et al. (2020)):

amplitude(olivine 1.0  $\mu\text{m}$  band) > 0.29

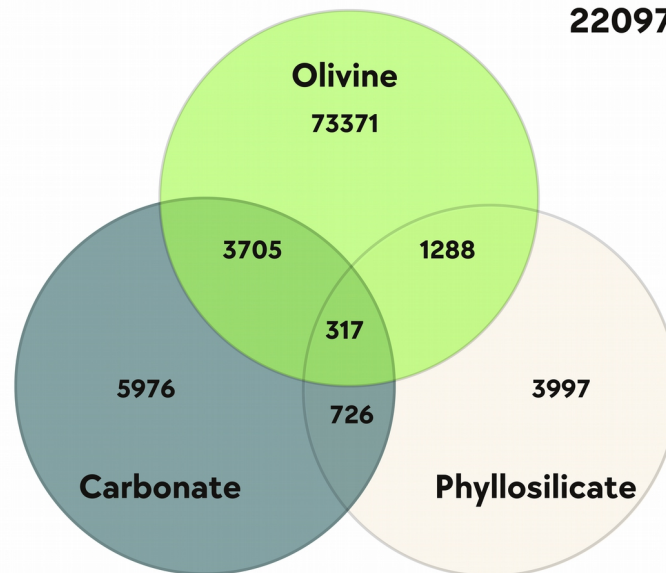
amplitude(carbonate 2.5  $\mu\text{m}$  band) > 0.08

amplitude(phyllosilicate 2.38  $\mu\text{m}$  band) > 0.065

For simplicity and reproducibility, these rules were run on the entire georeferenced HRL40FF CRISM image. No attempt was made (at first) to mask the image to regions of interest. We report the border pixels with no data as “edge pixels” and pixels with data as “ground pixels”.

**CRISM HRL40FF**

**341705 image pixels**  
**120727 edge pixels**  
**220978 ground pixels**



**No olivine,  
no phyllo, no carb:  
131598**

Figure 8. Venn diagram of olivine-phyllosilicate-carbonate detections for HRL40FF showing overlapping pixels containing olivine, phyllosilicate and carbonate. See text for details of calculation.

Figure 8 demonstrates that just more than half of the HRL40FF image is not



olivine, phyllosilicate or carbonate. Roughly one third of the ground pixels have olivine alone detected. “Pure” (i.e. without the other two minerals) phyllosilicate and carbonate are present in roughly 3% and 2% of the pixels, with carbonate being more abundant than phyllosilicate, using orbital data. This plot also demonstrates that there are large amounts of olivine without alteration, and small but significant amounts of phyllosilicate and carbonate without significant olivine signatures in the HRL40FF scene.

In order to take a closer look at the Séítah region as seen from orbit, we have subset the HRL40FF image to a smaller image of only 1750 pixels covering the Séítah region. Figure 9 displays the Venn diagram analysis for just this Séítah subset. This shows that the subset CRISM image mostly contains olivine (~95%), 2% of the pixels contain phyllosilicate and 1.5% are carbonates. Relative to the whole 40FF image, the Séítah subset contains far more pure olivine, but relatively smaller amounts of phyllosilicate and carbonate. This reflects the fact that the Séítah region carbonate and phyllosilicates are relatively difficult to detect from orbit. In the section that follows, we supplement these orbital data with in situ data from the Mars 2020 rover.

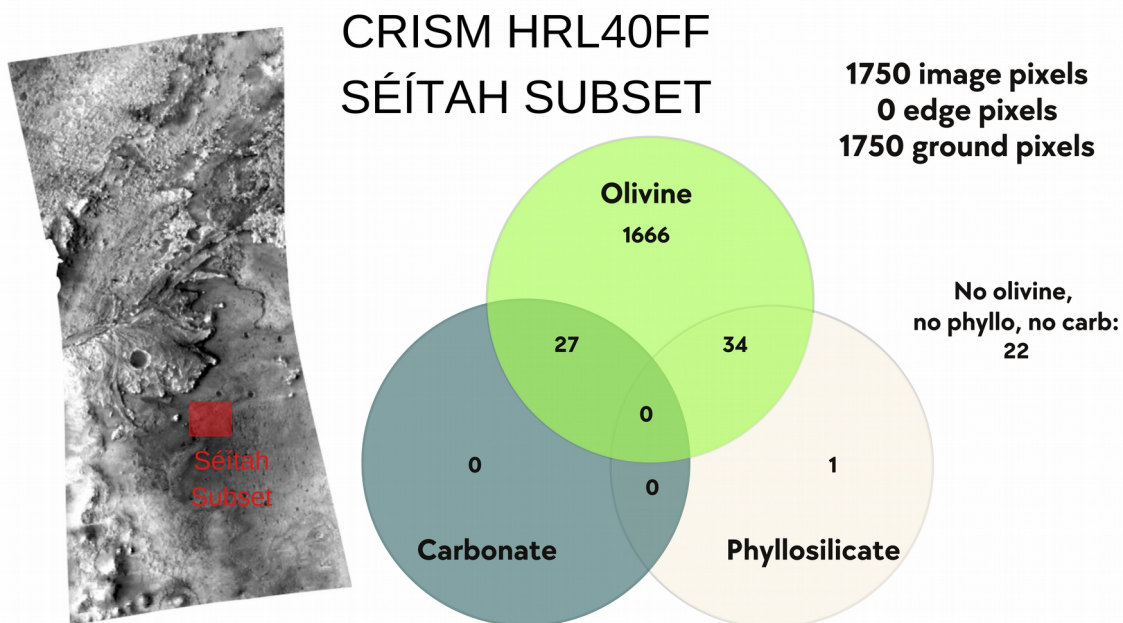


Figure 9. Venn diagram of olivine-phyllosilicate-carbonate detections for the Séítah subset of HRL40FF, which is shown in a red box in the image at left. The diagram on right shows overlapping pixels containing olivine, phyllosilicate and carbonate.

### 3.3.1 VISIR In situ results

Figure 10 shows the VISIR spectra from the abraded patch Garde taken on Sol 207 from the Séítah formation (Figure 1b). Absorption bands at 2.28, 2.33, 2.38 and possibly 2.46  $\mu\text{m}$  were detected. The lack of a moderate strength 2.5  $\mu\text{m}$  band suggests that this sample is not carbonate bearing; however, see the analysis by Clave et al. (this issue) in which LIBS and Raman techniques suggest small amounts of carbonate are present, and Corpolongo et al. (this issue) in which SHERLOC Raman analyses of the abrasion patch indicate carbonate. The presence of bands at 1.9, 2.28, 2.31, 2.38 and possibly at 2.46  $\mu\text{m}$  in the VISIR indicates that the Garde sample is phyllosilicate bearing. In addition, although weak, there is a band present in the spectra at 2.1  $\mu\text{m}$ , and though this is a little offset (2.09  $\mu\text{m}$ ), it is also present in talc. Finally, the 2.46  $\mu\text{m}$  band in serpentine is far weaker than in talc. Figure 10 also shows the example of a spectrum from Dourbes\_Tailings\_255 which shows the most convincing example we have found of bands at 1.94, 2.28, 2.31, 2.38 and at 2.46  $\mu\text{m}$ , thereby constituting the strongest evidence so far in the Séítah formation for the presence of talc.

Also shown in Figure 10 are talc, serpentine (lizardite), hectorite, saponite, Fe/Mg smectite and stevensite spectra from Figure 4 for direct comparison with the band positions of the VISIR data.

Table 2 is a summary of the band positions that are present in each of the minerals and targets that are present in Figure 10. Red text indicates a band is weak or missing in this location. An asterisk indicates the presence of a shoulder band.

Table 2. Assessment of SWIR band positions for elements in Figure 10. All values are in  $\mu\text{m}$ . Asterisk indicates bands, red text indicates missing or weak band.

Target	1.9-1.97	2.0-2.1	2.1-2.16	2.25-2.29	2.29-2.35	2.35-2.40	2.40-2.5
Garde 207	1.94	2.08	2.14	2.28*	2.32	2.39	2.46
Dourbes Tailings 255	1.94	2.08	2.14	2.28*	2.32	2.39	2.46
Talc TL2702	1.91	2.08	2.14	2.28*	2.31	2.39	2.46
Lizardite NMNHR4867	1.97	2.08	2.14	2.29*	2.32	2.39	2.46
Fe/Mg Smectite	1.91	2.08	2.14	2.28	2.32*	2.39	2.46
Hectorite	1.91	2.08	2.14	2.29*	2.31	2.39	2.45
Saponite	1.91	2.08	2.14	2.29*	2.31	2.39	2.46
Stevensite	1.91	2.07	2.12	2.29*	2.31	2.39	2.47



677 Based on Table 2, the lack of a 2.46  $\mu\text{m}$  band is somewhat problematic for lizardite  
678 and Fe/Mg smectite, however the 2.46  $\mu\text{m}$  band in Dourbes is so weak that it can  
679 hardly be disqualifying. At this stage, we see advantages to keeping all 6 candidate  
680 minerals in the mix, in the anticipation of spectra with stronger absorption bands in  
681 the Marginal Carbonates region.

682

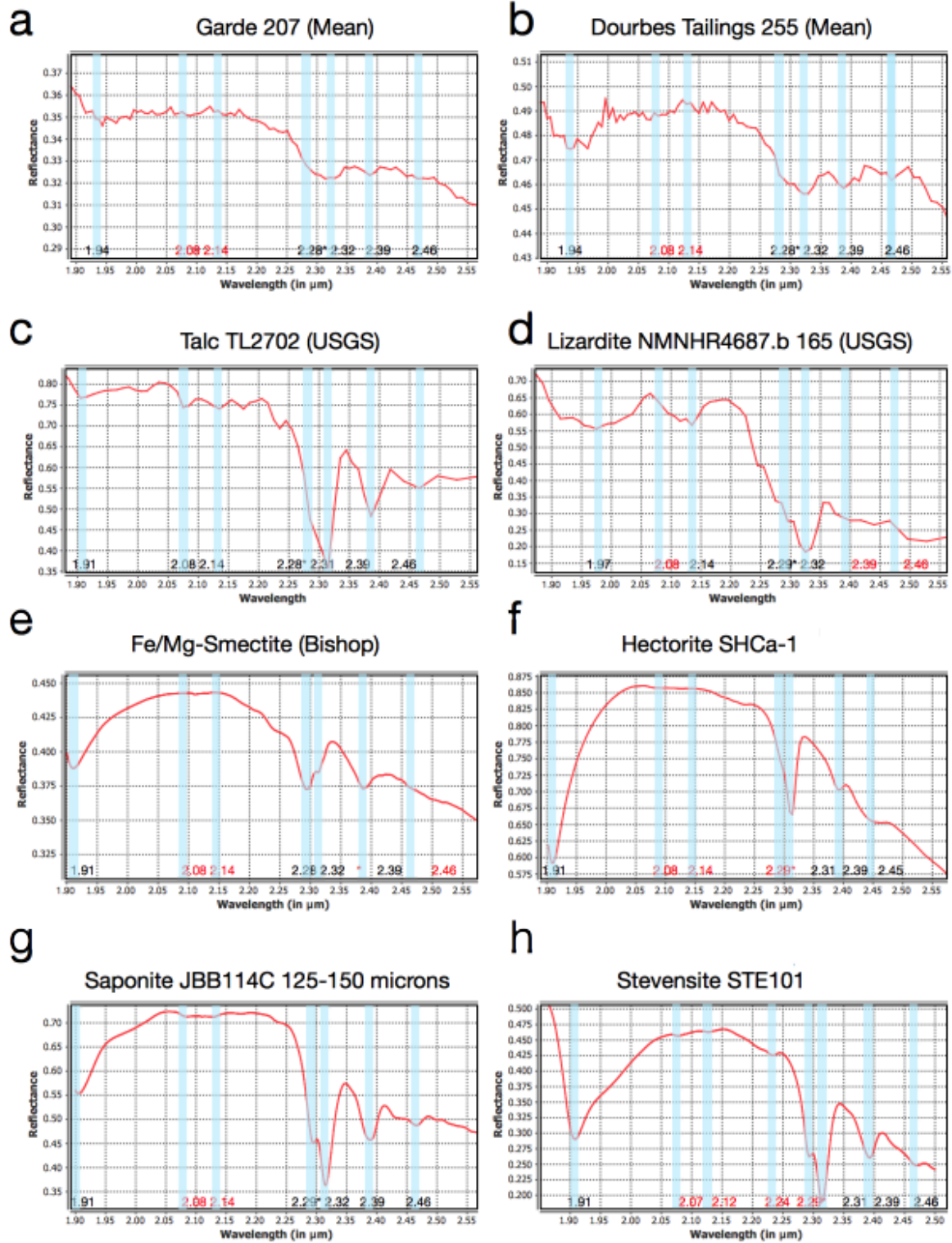
683

684

685

686

687



692  
693  
694  
695  
696  
697  
698

699 *3.3.2 VISIR, RMI and Mastcam-Z tailings observations*  
700

701 Figure 11 shows the MastCam-Z image for the Dourbes target (abraded rock,  
702 Figure 1c), showing the tailings that were captured by the VISIR instrument. It  
703 should be noted that the tailings are relatively bright, especially compared with the  
704 surrounding bedrock, which is again consistent with the presence of talc or  
705 hectorite, which both have high reflectance ( $>0.9$  in the visible region). It should  
706 be noted that a decrease of grain size will also increase the albedo, so we do not  
707 consider the brightness change to be definitive evidence for talc/hectorite over the  
708 other phyllosilicates.

709

710 Also shown in Figure 11 are the spectra from the VISIR observations of targets  
711 Dourbes, Salette and Brac, which are shown with the spectra of the original rock  
712 surface and the tailings after abrasion. The key thing to note, particularly in the  
713 Dourbes example, is the relative overall increase in albedo, and the appearance of a  
714 band at  $2.46\text{ }\mu\text{m}$  which is not present (or only weak) in the original rock. This is  
715 strongly suggestive that the tailings have made the presence of the phyllosilicate  
716 more obvious in the spectra, and because the  $2.46\text{ }\mu\text{m}$  band is not present in  
717 lizardite (Figure 10), this also suggests the tailings contain the mineral talc.

718  
719  
720

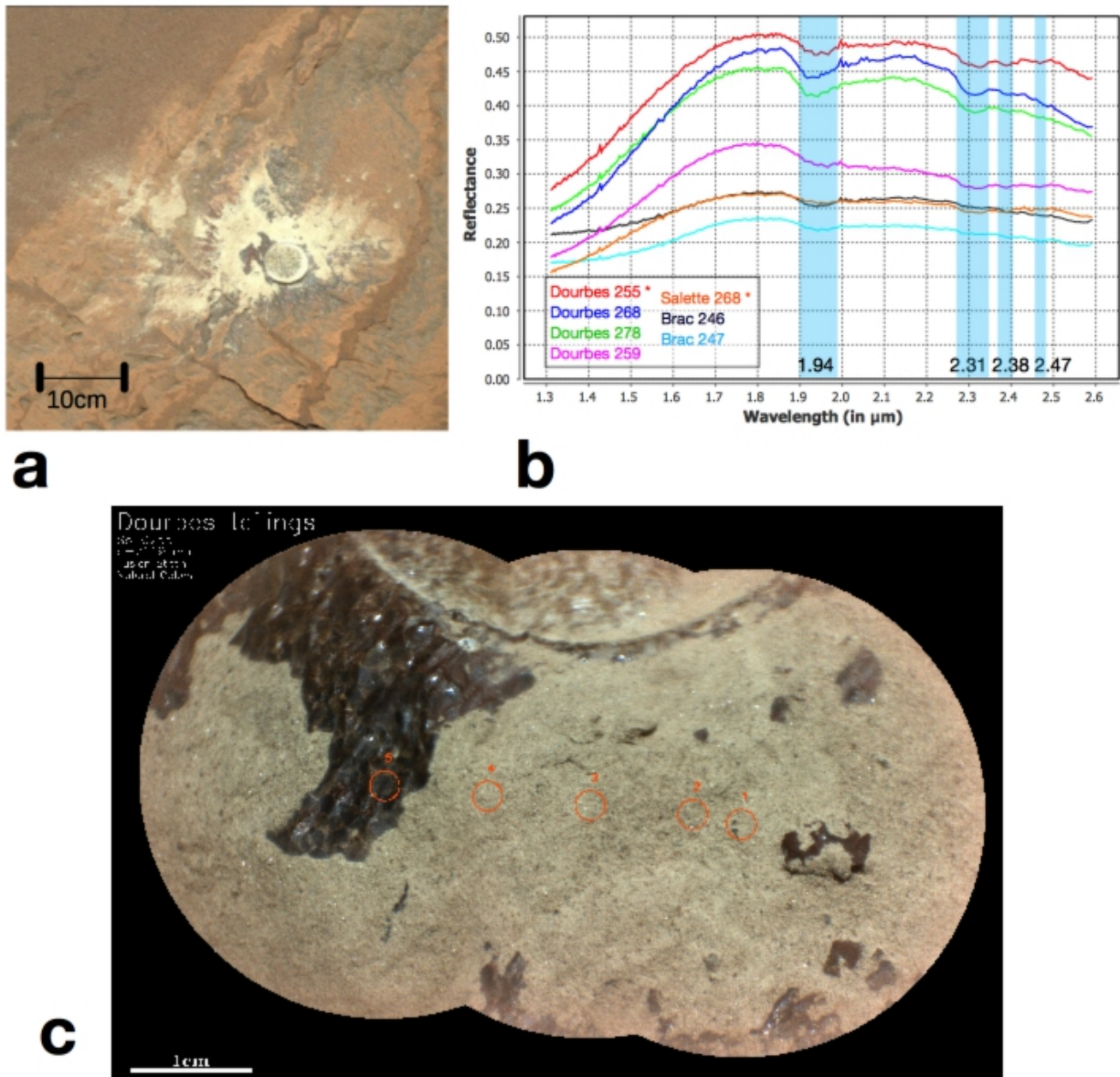
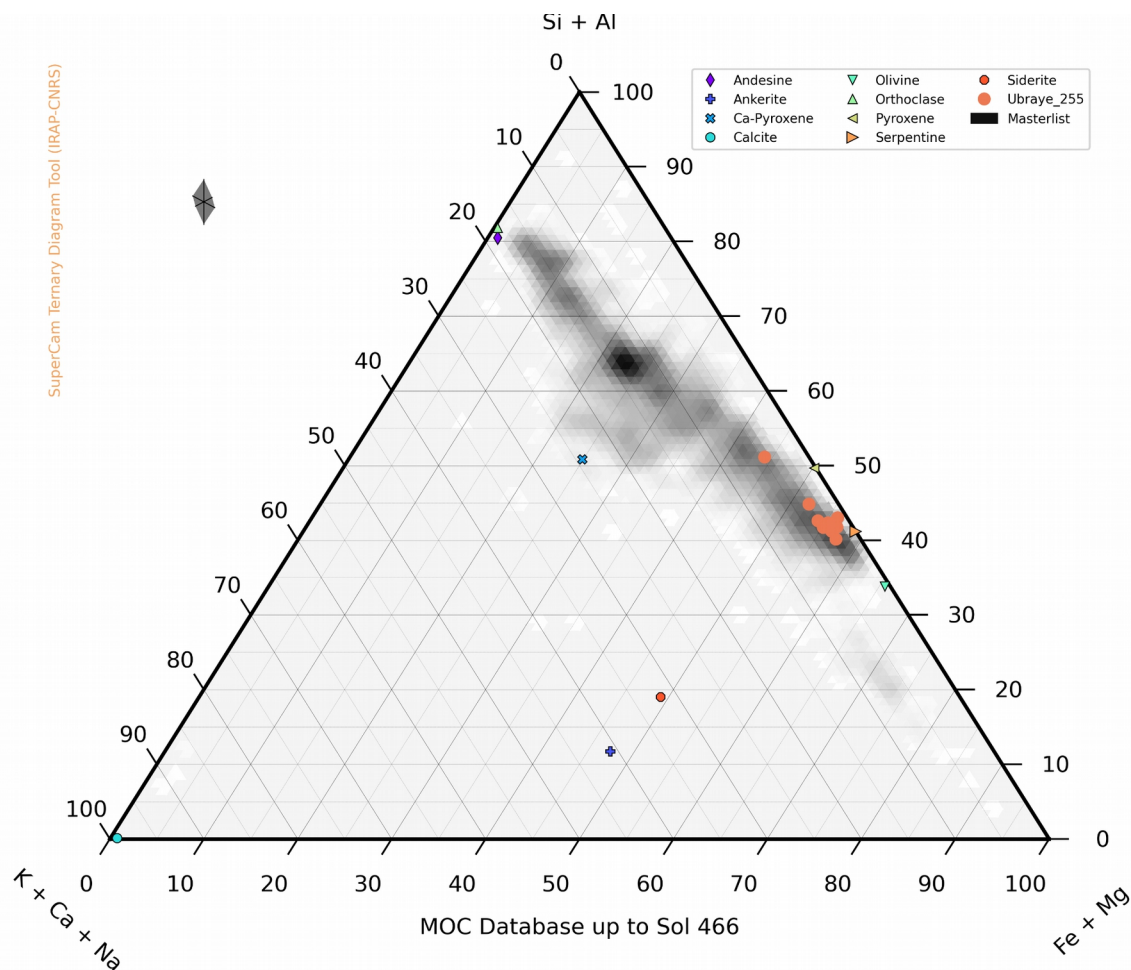


Figure 11. a.) Mastcam-Z of Target Dourbes with tailings on Sol 255 after abrasion in the Brac workspace. Note the brightness of tailings compared to the original rock surface. For scale, the abrasion patch is 5cm across. b.) Spectra of the tailings compared to the original rock surface. Spectra of tailings are marked with an asterisk (\*). Note the presence of the 2.46  $\mu\text{m}$  band in the tailings spectra c.) SuperCam RMI image of target Dourbes tailings after abrasion. The numbered red circles indicate the locations at which the data was taken for the Dourbes 255 tailing target and their fields of view (65% of total signal encircled). The blue spectrum in (b) corresponds to the average of the red circles in (c).

### 731 3.3.3 SuperCam LIBS ternary plot

732 Figure 12 shows a Si+Al-Fe+Mg-Ca+Na+K ternary diagram displaying the  
 733 SuperCam LIBS elemental composition results up to Sol 466 of the mission in  
 734 black/grey and 10 orange points measured on the target Ubraye\_255 which is a  
 735 rock showing cumulate texture located near the Dourbes abrasion patch in the Brac  
 736 workspace (Figure 1c). The elemental composition lies very close to the olivine  
 737 calibration target and also overlaps with the region of talc and serpentine. Given  
 738 how close these points are and the errors inherent in the planetary LIBS  
 739 observations (Anderson et al., 2022) it can become challenging to tell these  
 740 mineral compositions apart by just looking at the major elements. We provide in  
 741 the supplementary section S3 a discussion of errors and discrimination of points in  
 742 the ternary plot.



743

744 Figure 12. LIBS and geochemistry ternary molar plot indicating Ubraye\_255 (orange circles without  
 745 outline) cumulate target showing overlapping olivine (green inverted triangle) and serpentine (right-  
 746 pointing orange triangle) standards on board the rover. The gray polygon at top left above the main figure  
 747 indicates the precision error bars of the plot.



748 Table 3 gives an example composition from Cine and Ubraye showing the very  
749 low (<4 wt %) Al present in these samples. Anderson et al. (2022) Table 5 gives the  
750 mean accuracy of the Al<sub>2</sub>O<sub>3</sub> estimate at +/- 1.8wt %. For these LIBS targets  
751 (Cine/Garde, Udraye/Dourbes which are all in the Séítah region) we can thus  
752 eliminate the possibility of Al-bearing phyllosilicates.

753

754

755

756

757

758

759

760

761 Table 3. SuperCam LIBS Elemental abundances from targets Cine\_206 (cumulate rock next to Garde in  
762 Bastide workspace) and Ubraye\_255 (cumulate rock near Dourbes in Brac workspace). Cine\_206 point 3  
763 and 5 and Ubraye\_255 points 1-4 and 6-10 show a very low amount of Al to within error (<4%) in the  
764 cumulate textured rocks. Green boxes highlight the high values of FeO<sub>T</sub> and MgO and red boxes highlight  
765 the low values of Al<sub>2</sub>O<sub>3</sub>. S.D. is the standard deviation for that elemental data. Specifically, it is the S.D.  
766 of the 25 single shot spectra averaged in each case. All elemental abundance data are in wt %.

		SiO <sub>2</sub>		Std																									
Target	#	SiO <sub>2</sub>	S.D.	TiO <sub>2</sub>	Dev	Al <sub>2</sub> O <sub>3</sub>	S.D.	FeO <sub>T</sub>	S.D.	MgO	S.D.	CaO	S.D.	Na <sub>2</sub> O	S.D.	K <sub>2</sub> O	S.D.	Total											
Cine	1	44.99	1.19	0.43	0.02	3.27	0.53	13.37	1.52	11.54	1.16	15.84	0.68	0.39	0.13	0	0.17	89.83											
Cine	2	51.05	1.9	0.04	0	2.94	0.97	25.74	2.06	13.4	1.96	4	0.5	1.19	0.38	0	0.15	98.36											
Cine	3	45.13	2.03	0.01	0.02	0.87	0.95	34.59	2.13	28.93	1.27	1.81	1.09	0.37	0.33	0	0.05	111.7											
Cine	4	43.39	1.15	0.45	0.03	3.91	1.34	10.43	2.41	11.13	0.92	13.72	0.79	0.49	0.17	0	0.19	83.52											
Cine	5	45.34	2.14	0.01	0.01	2.89	1.08	36.37	3.56	28.35	2.22	1.28	0.48	0.51	0.11	0	0.03	114.7											

767  
768

		SiO <sub>2</sub>		Std																									
Target	#	SiO <sub>2</sub>	S.D.	TiO <sub>2</sub>	Dev	Al <sub>2</sub> O <sub>3</sub>	S.D.	FeO <sub>T</sub>	S.D.	MgO	S.D.	CaO	S.D.	Na <sub>2</sub> O	S.D.	K <sub>2</sub> O	S.D.	Total											

Ubraye_255	1	48.72	2.07	0.01	0	2.02	0.88	24.5	2.92	31.5	0.85	1.43	0.54	1.22	0.21	0	0.23	109.4
Ubraye_255	2	44.76	2.2	0.01	0	2.25	0.88	25.94	2.24	27.91	2.7	1.25	0.37	0.34	0.09	0	0	102.46
Ubraye_255	3	51.41	2.57	0.02	0.01	1.57	1.06	23.63	3.05	32.07	0.85	0.8	0.4	1.37	0.17	0.49	0.41	111.36
Ubraye_255	4	45.97	1.52	0.01	0	1.79	0.75	26.35	2.87	28.87	2.03	1.32	0.36	0.3	0.1	0	0.03	104.61
Ubraye_255	5	49.34	2.74	0.04	0	3.92	1.14	28.53	3.78	15.25	2.62	1.65	0.44	1.32	0.14	0.52	0.38	100.57
Ubraye_255	6	46.36	1.4	0.01	0	1.78	1.11	21.35	1.86	30.32	1.16	0.56	0.21	0.29	0.05	0	0.15	100.67
Ubraye_255	7	43.03	7.28	0.03	0.01	2.59	1.32	27.74	3.44	26.59	0.89	1.52	0.42	0.65	0.13	0	0.12	102.15
Ubraye_255	8	47.04	1.74	0.01	0	1.67	0.72	23.18	2.38	29.89	1.04	1.41	0.34	0.65	0.17	0	0.07	103.85
Ubraye_255	9	45.92	2.24	0.49	0.11	3.47	0.79	25.17	2.79	24.79	0.66	1.53	0.3	0.97	0.18	0	0.04	102.34
Ubraye_255	10	45.84	2.18	0.01	0.01	0.54	0.67	27.48	2.68	28.97	2.2	1.46	0.21	0.76	0.15	0	0.03	105.06

769

770

771

772

773

774

775

776

4. Discussion

777

778

779

780

781

782

4.1 Emplacement of olivine-phyllsilicate-carbonate lithology and exposure today

783

784

785

786

787

788

789

Flood lavas (e.g. the Columbia River basalt) are characterized by 1) large spatial extent, 2) low viscosity, 3) relatively thick (5-45 m) flows 4) fed by fissure eruptions which are covered by the erupting lava (Plescia, 1990). This is in contrast to (or could evolve over time to) plains lavas (e.g. Indian River basalt), which have smaller-extent, higher-viscosity, thinner flows accompanied by low shields (Plescia, 1990).

790

791

792

793

794

795

796

797

Given the low viscosity for the lithology calculated in this paper, the results of RIMFAX (the Ground Penetrating Radar instrument on the Mars 2020 rover) showing the relatively thick flows (Hamran et al. 2022) , and the lack of low shields in the region from orbital mapping, we consider it likely the olivine-phyllsilicate-carbonate at the Séítah formation was emplaced as a flood lava. Future observations at the Marginal Carbonates and outside Jezero will test what other formation mechanisms are involved in other parts of the lithology.

Under the flood lava hypothesis, the olivine-phylllosilicate-carbonate lithology was likely variable in thickness, and in catchment regions of deep relief, such as Jezero crater, the flow formed a lava lake several decimeters thick.

*Effect of viscosity.* Worster et al. (1993) presented a model of heat flow in a lava lake cooled from above and insulated (or cooled) from below, and utilizing the balancing of the heat equation with crystallization of the melt, they could estimate the total crystallization amount. Their results are shown with their model in Figure 3. Figure 3b also shows that for inferred viscosities typical of the Séítah elemental composition, using the two base cooling scenarios as error bounds, the formation of crystals could have filled up to  $\sim 40\% \pm 10\%$  of the volume of the lake.

Very fluid lava flow episodes have been described in the case of rather recent volcanic events at Central Elysium Planitia (Vaucher et al., 2009) and Tharsis region (Mangold et al., 2010). The combined mineralogical and petrophysical information gained at Jezero with this current study of Séítah unit points to the fact that low viscosity lava flows did occur, possibly at large scale, early in the martian history; as such, it may place valuable constraints on the ultramafic composition of the Martian interior at a rather early to intermediate stage of chemical differentiation.

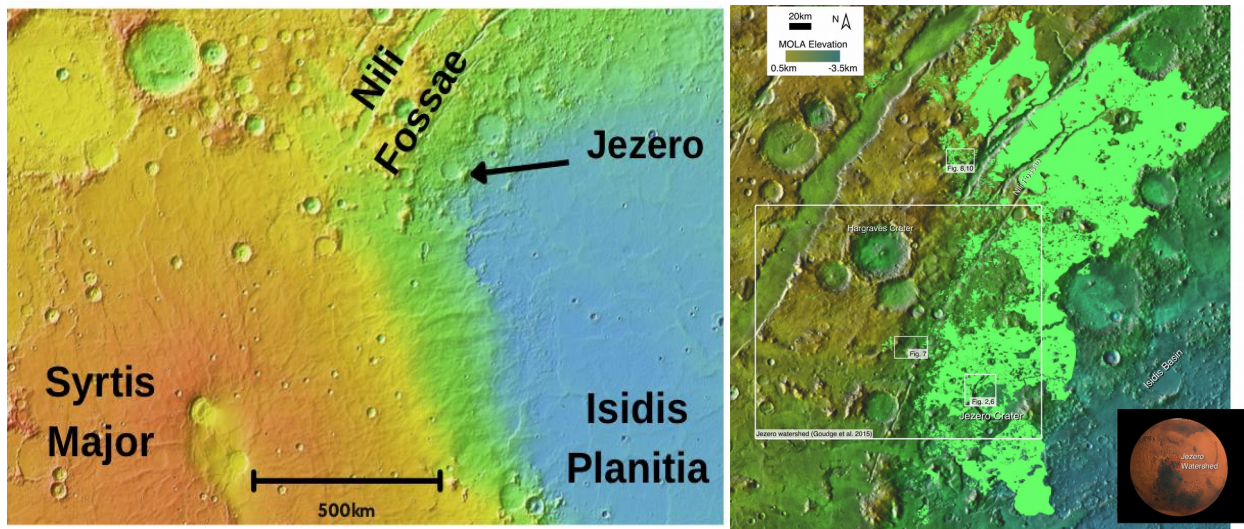
*Depth of lava lake.* We suggest that the lava lake has been eroded back to reveal the cumulate portion of the lava lake and then covered by crater fill consisting of igneous material from later eruptions such as the Máaz formation (Udry, this issue) and Artuby member of the Máaz unit (Alwmark, this issue) which has itself then been eroded back in locations to reveal the olivine-phylllosilicate-carbonate beneath it (Hiesinger and Head, 2004; Goudge et al., 2015). Ground-penetrating radar imaging performed by RIMFAX in the vicinity of Séítah reveal sub-horizontal high-amplitude reflectors down to 15 m burial depth including lenticular reflector geometries interpreted to most likely represent cross-sections of igneous flow lobes (Hamran et al., 2022) The base of the Séítah unit currently remains unclear, but is at least  $\sim 15$  m below the surface at the deepest locations observed so far by RIMFAX.

Assuming for the sake of the argument that the Séítah formation was  $\sim 10$  m deep if it was formed as a lava lake, this suggests (using Figure 3b) that approximately the lower  $\sim 4 \pm 1$  m consists of the cumulate Bastide workspace (Figure 1b) in which Cine\_206 and Garde\_207 were observed.

#### *4.1.1 Spatial distribution of lithology as flood lava*

838

839 Wilson and Head (1994) pointed out that lava flows on Mars will extend roughly  
 840 six times further than lava of the same composition on Earth. as mentioned in  
 841 Section 2, this is due to the lower gravity and the lower pressure of the current  
 842 Martian atmosphere. A higher pressure Noachian atmosphere would decrease the  
 843 runout. The emplacement of the lava that created the Séítah formation olivine  
 844 cumulate covered a significant portion of the planet (Figure 13). Kremer et al.  
 845 (2019) mapped the unit to extend over both sides of the Nili Fossae, and showed  
 846 the unit to be predominantly exposed on the eastern side of the Nili Fossae, and  
 847 truncated by Syrtis Major to the south, and later cratering activity, most notably by  
 848 Hargraves Crater in the middle of the two predominant Fossae. Considering only  
 849 the region of the Isidis Planitia basin complex currently covered by the olivine-  
 850 phyllosilicate-carbonate unit, and excluding the olivine on the Libya Montes region  
 851 on the southern edge of the basin, this area extends roughly 500 km north to south  
 852 and 350 km east to west and is approximately the size of Florida (in 2022) in the  
 853 United States ( $\sim 170,000 \text{ km}^2$ ).  
 854



855

856 Figure 13. a.) MOLA image showing the relationship of western edge of the Isidis Basin complex, giving  
 857 the relative positions of Syrtis Major, Nili Fossae and Jezero Crater. b.) Figure 1 of Brown et al. (2020)  
 858 showing the extent of the olivine-phyllsilicate-carbonate lithology as mapped by Kremer et al. (2019) in  
 859 a region about the size of Florida. Note obscuration by later crater ejecta blankets, especially Hargraves  
 860 Crater.  
 861

862

862 The direct contact between the Syrtis Major lavas and the olivine-phyllsilicate-  
 863 carbonate is striking and leads one to conjecture whether the Fossae extends  
 864 beneath the Syrtis Major construct; although this has not been previously  
 865 addressed, we will now postulate about how this geophysical relation might have  
 866 occurred. Rampey and Harvey (2012) identified the wide depressed footprint of

867 Syrtis Major and suggested that:

868 “early eruptions at Syrtis Major might have consisted of voluminous low-  
869 viscosity, possibly komatiitic magmas, whose powers of thermal erosion  
870 ... may have been responsible for the wide, depressed footprint of Syrtis  
871 Major.”

872 And at the end of the same paragraph:

873 “... the youngest and most visible surface rocks of which would be  
874 basaltic komatiites, but whose earlier, more voluminous rocks would have  
875 been ultramafic. In the absence of tectonic effects these deep-seated rocks  
876 would have restricted exposure.”

877 We would contend that the missing earlier, more voluminous ultramafic rocks, are,  
878 in fact, the olivine-phyllsilicate-carbonate lithology we have been studying.  
879 Somewhat more speculatively, we might make some passing comments which may  
880 be useful for the collective consciousness to test in future investigations. The  
881 suggestions are four-fold and currently have no basis in observation, but are  
882 consistent with observations so far and may be tested in future observations, for  
883 example when the *Perseverance* rover can inspect the Nili Fossae in situ.

884

885 1) The fissures that were the source of the olivine-phyllsilicate-carbonate lava  
886 were possibly linked to, or in fact used, the Nili Fossae fractures on the northwest  
887 of Isidis Planitia, and opened after the Isidis impact (Wichman and Schultz, 1989).  
888 The analogy might be made to the relationship between Cerberus Rupes and  
889 Cerberus flood lavas (Plescia, 1990) in Central Elysium Planitia.

890 2) At Cerberus, it is possible that the flood lava evolved to a plains style lava. This  
891 may also have happened in the Isidis basin, where Syrtis Major may have been  
892 created after fissure lavas became more viscous, and the Syrtis shield may now  
893 cover fissures from an earlier phase of flood volcanism that produced the olivine-  
894 phyllsilicate-carbonate lithology. Figure 13 shows a Mars Orbiter Laser Altimeter  
895 (MOLA) altimetry map of the region highlighting the spatial relationships between  
896 the Isidis, Syrtis, Nili Fossae and Jezero crater. Rampey and Harvey (2012)  
897 suggested that Syrtis Major evolved from ultramafic to mafic over time and that  
898 super-hot komatiite lava may have eroded basement rocks. As noted by previous  
899 authors, no olivine has been found to date in the Fossae floor or walls (Hamilton  
900 and Christensen, 2005; Mustard et al., 2007). However, it is possible that evidence  
901 of this olivine may yet be found buried at depth by Syrtis Major lavas. Channelized  
902 lava flows travel much further than non-channelized flows (Pinkerton and Wilson,  
903 1994), and the last Syrtis Major lavas may have traveled more easily in the Nili  
904 Fossae graben and subchannels.

905 3) At Cerberus, the lavas are much younger than the olivine-phyllsilicate-  
906 carbonate, post-date water-related fluid channels, and are often guided by those



channels. Volcanic activity commenced at Syrtis between 3.6-3.9 Ga (Robbins et al., 2011) around the same time as the oldest deposits on Tharsis were emplaced at 3.67 Ga (Isherwood et al., 2013). The age of the olivine-phylllosilicate-carbonate (3.82 +/- 0.07Ga, Mandon et al. (2020)) would imply that no surface water channels were available to confine the flow, but might instead be governed by the widespread emplacement of the Noachian basement rocks.

4) During emplacement of this super-hot lava lake, it might be possible that Séítah sank into and eroded the regolith it was laid down upon (Huppert et al., 1984). Evidence for all four of these suggestions might be found in exposures sounded by RIMFAX during the Mars 2020 mission in the Outside Jezero part of the mission.

#### *4.1.2 Properties of cumulate layer and terrestrial analog*

Huppert and Sparks (1981) discuss the manner in which an olivine bearing ultramafic cumulate layer might form in a magma body beneath a less dense plagioclase bearing basaltic layer. This model is a reasonable candidate for the formation of the Séítah formation and the Artuby member of the Máaz formation (see also Crumpler et al., this issue). It may even be possible that the lava which formed Séítah was contaminated during eruption and emplacement (Huppert and Sparks, 1985), and given its low viscosity and high temperature, this may have differentiated the upper Issole member as a contaminated version of the lava producing the lower cumulate Bastide member (Crumpler et al., this issue).

Figure 14 compares the Martian olivine cumulate target Cine\_206 and the terrestrial olivine cumulate target AJB0503100 from the Dresser Formation in the Pilbara Craton of Western Australia. Both show equant (1 to 1.5 mm diameter) grains that are interlocking. Both were likely formed as the basal part of a lava flow or ponded lake when the olivine crystals fell out of suspension and collected at the basal cumulate layer. The terrestrial example on the right was sampled from the talc-carbonate altered unit at the bottom of the Mt Ada Basalt in the Dresser Formation of the North Pole Dome in the Pilbara region of Western Australia. The sample is part of a komatiite sequence and specifically the B2 adcumulate layer (Arndt et al., 2004). We have shown in this paper that the target Cine shares many spectral, mineralogical and morphological characteristics of the terrestrial target.

Although a Martian lava lake is likely to have formed from a cooler mantle source than the terrestrial komatiite (Putirka, 2016), we contend that it is the viscosity we have derived here that governs emplacement properties of the lava flow. Direct comparison of the viscosity of the two units is challenging due to the high Mg nature and alteration of the terrestrial sample (MgO 18.9 wt.%, FeO<sub>T</sub> 7.6 wt.% from microprobe, presented in Brown (2006)) versus the higher Fe content of Target Cine (SiO<sub>2</sub> 45.24 wt %, MgO 28.64 wt.% and FeO<sub>T</sub> 35.48 wt.%, which is the average of Cine points 3 and 5 from Table 3). It should be noted that both these rocks do not have a true bulk rock content because they are cumulates of material that were sourced from elsewhere, most likely within the upper zone of the lava lake.

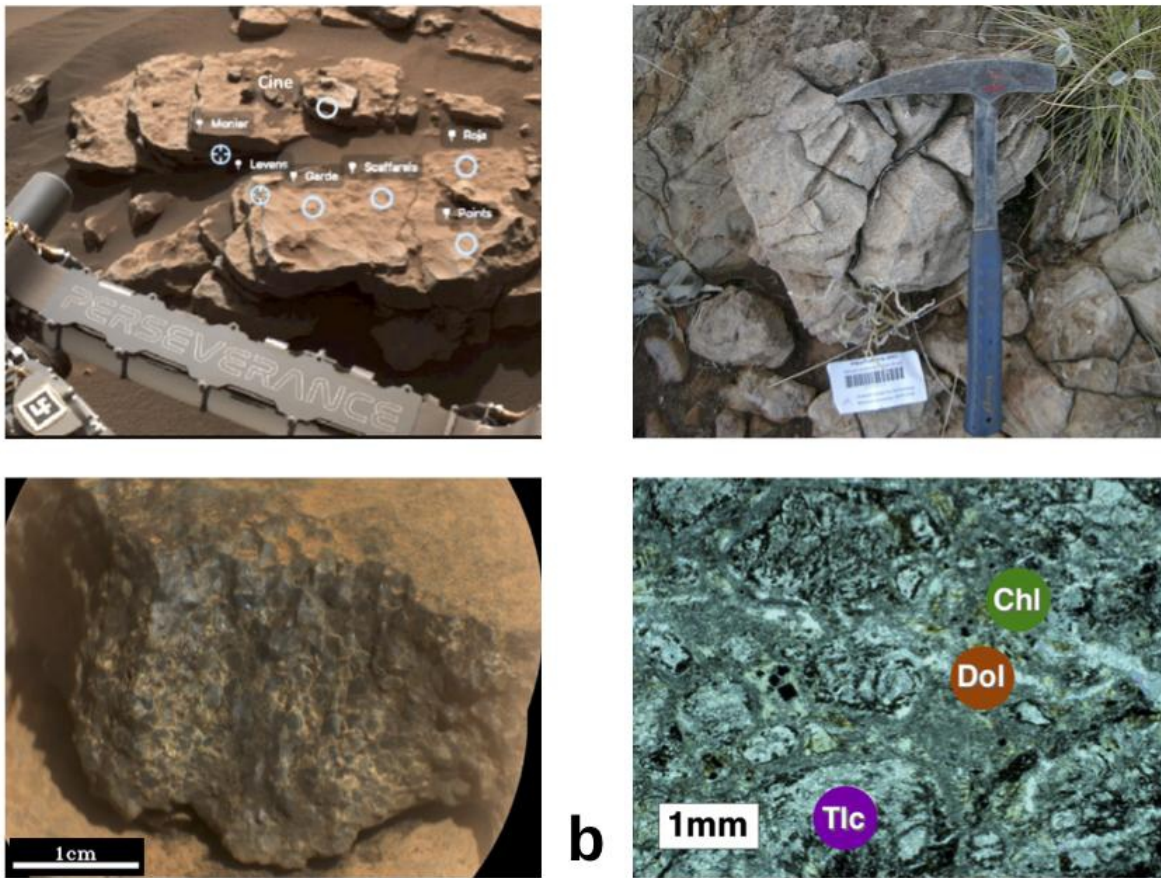


Figure 14. a.) (bottom) SuperCam RMI of target Cine showing olivine cumulate texture at mm scale. (top) Bastide workspace, location of Cine relative to Garde, rover arm for scale. b.) (bottom) Thin section of talc-carbonate sample AJB0503100 from Brown (2005; 2006) with mm size talc (Tlc) replacing olivine, dolomite (Dol) and chlorite (Chl) identified using electron microprobe. (top) Context image for target AJB0503100 with hammer for scale.

#### 4.2 Post emplacement phyllosilicate-carbonate alteration

The fact that ~3.94 Ga olivine is still well preserved on Mars and relatively unaltered speaks volumes to the amount of alteration and volatiles present on the fourth planet. In terrestrial greenstone Archean terranes, olivine is usually only present as a polymorph of its former self, often replaced by phyllosilicates such as serpentine or talc (Figure 14b).

Wilson and Head (1994) suggest that lavas on Mars have fewer volatiles than lavas on Earth. Despite this, the low amount of alteration present means it is still possible that the alteration fluids were juvenile water and CO<sub>2</sub>, sourced from the fissure, as suggested and discussed by Brown et al. (2020).

The limited extent of post emplacement phyllosilicate and carbonate alteration is evident from the Venn diagrams we have presented in Figures 8 and 9, and is also the subject of two studies, including phyllosilicate (Mandon et al., this issue) and carbonate (Clave et al., this issue). Mandon et al. (2022) show that in olivine-carbonate-serpentine mixtures, the bands of serpentine are deep for percentages of < 5 wt.% of serpentine. This also has implications for the alteration history, as the rocks in the Séítah formation might not have extensively interacted with fluid compared to some other parts of the regional olivine unit, which appear more altered from orbit.

#### *4.3 Other emplacement models*

There are a number of aspects of the regional morphology and properties of the olivine-phyllosilicate-carbonate lithology that remain poorly understood, including draping morphology and laterally continuous layering and lack of clear lobate features. These have been used to argue in favor of an explosive volcanic origin for the lithology (Rogers et al., 2018; Kremer et al., 2019; Mandon et al., 2020; Ruff et al., 2022). Ravanis et al. (2022) report on modeling to determine grain sizes for Martian Nili Fossae ashfall deposits in order to better understand the potential for pyroclastic fall deposits to be emplaced away from the eruption source. Wilson and Head (1994) modeled clasts with diameters between 100 µm and 10 mm and maximum travel ranges of pyroclasts in current day (6 mbar) Martian atmosphere for eruption cloud heights from 50-300 km. Their Figure 21 demonstrated that the maximum range drops sharply as grain size increases. They also presented a modeled maximum pyroclastic flow run out length as a function of eruption velocity for three different surface friction coefficients. Their Figure 23 shows that the 1.5 mm olivine grain size would only travel about 20 km away from the vent through pyroclastic fall, and thus far, the Mars 2020 team is yet to discover

1008 pyroclastic signatures (e.g. fiamme) in the imagery of abrasion patches obtained by  
 1009 the rover.

1010

#### 1011 *4.4 Future prospects and Mars Sample Return*

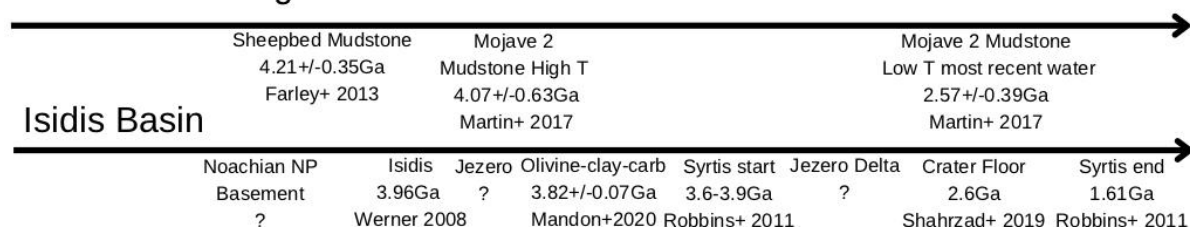
1012

1013 At the time of writing this paper and other accompanying papers in the Jezero  
 1014 Crater Floor collection, the ongoing progress of the *Perseverance* rover has  
 1015 brought it to the Jezero Delta campaign of its mission. Within the delta, the delta  
 1016 curvilinear unit (*DCu*) and some parts of the delta have been documented to  
 1017 contain carbonates, from orbital studies (Goudge et al., 2015, 2018), and are now  
 1018 being characterized by surface observations (Mangold et al., 2021). We anticipate  
 1019 unexpected findings in the rocks and cobbles of the delta, which will provide us  
 1020 views of the outside watershed at irregular intervals. Figure 15 gives the timeline  
 1021 of events in Martian geological history that are critical to understanding its  
 1022 evolution and reliance upon regional and global events. We point out that this  
 1023 timeline shows an approximate correlation between the Jezero Delta and the  
 1024 recently hypothesized second generation ocean, called Deuteronilus, aged  
 1025 approximately at 3.65Ga, and discussed in Citron et al. (2018) which they  
 1026 hypothesized filled Isidis with water. The existence and timing of these oceans is a  
 1027 source of ongoing debate (Sholes et al., 2021; Sholes and Rivera-Hernández, 2022)  
 1028 and during the Delta campaign we may hope to deepen our understanding of the  
 1029 source of the water that once filled Jezero.

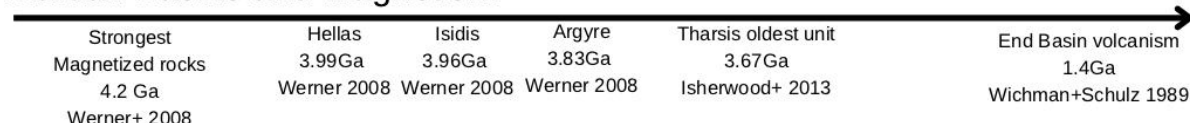
1030



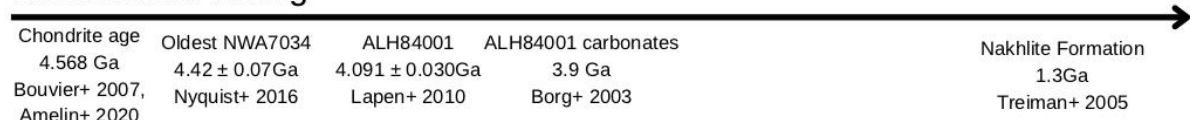
## Gale crater dating



## Martian Basins and Magnetism



## Radiometric dating



## Putative Ocean shorelines



Figure 15. Timeline of events relevant to the emplacement and retention of the olivine-phyllsilicate-carbonate lithology. Dates are from various sources (Amelin et al., 2002; Borg et al., 1999; Citron et al., 2018; Farley et al., 2013; Isherwood et al., 2013; Lapen et al., 2010; Mandon et al., 2020; Martin et al., 2017; Nyquist et al., 2016; Robbins et al., 2011; Shahrazad et al., 2019; Treiman, 2005; Werner, 2008; Wichman and Schultz, 1989). NP = Nili Planum

After the Delta campaign, the rover will pass either nearby or through the marginal carbonates, which are the greatest concentration of carbonates at Jezero (Figure 6).

Throughout its mission *Perseverance* is collecting samples for later return to Earth as part of the Mars Sample Return Mission. The samples collected in the Crater Floor campaign are discussed in Simon et al. (this issue). Upon return to Earth, we anticipate these activities to test the postulates and expand the findings of this paper:

- \* Use of radiometric age dating on the grains and mesostasis,
- \* Determination of phyllosilicate and carbonate type using Microprobe and X-ray Diffraction,
- \* Determination of phyllosilicate and carbonate relative timing using X-ray tomography,
- \* Source of carbonate using stable isotopes,



\* Age dating of delta topsets and bottom sets samples to constrain the age of the Jezero Delta.

## 5. Conclusions

The *Perseverance* mission completed the Crater Floor science campaign in April 2022, and thus the observations and interpretations we have reported here are limited to the olivine-phyllsilicate-carbonate as it appears at the Séítah formation. We can infer characteristics of the unit beyond Jezero based on orbital observations (Goudge et al., 2015; Horgan et al., 2020; Mandon et al., 2020; Brown et al., 2020). For example, one observation of the orbital data demonstrated that the largest olivine spectral features (and inferred grain size) are found outside, and to the north, of Jezero (Brown et al., 2020). However, our findings for this regional lithology will remain uncertain until we are able to reach these locations for in situ observations. These occasions will no doubt be as informative as the visit of *Perseverance* to Séítah.

We have made the following new findings and interpretations:

1. We have used a Venn-diagrammatic approach to establish that the previously identified “olivine-carbonate” lithology should actually be called the “olivine-phyllsilicate-carbonate” lithology.
2. Again using the Venn-diagrammatic approach, we have demonstrated the limited extent of alteration by phyllsilicate and carbonate, particularly for the Séítah subset of HRL40FF.
3. We propose that the olivine-phyllsilicate-carbonate lithology at the Séítah formation was emplaced as a flood lava, with low viscosity, relatively deep flows, and lack of low shield volcanoes.
4. We have presented a model suggesting that thermal-convection-driven cooling, balanced by crystallization of the lava, may have taken place in order to form large mm-sized crystals seen in the Séítah formation.
5. We have presented a model where flood lava ponded into a lava lake in Jezero crater, and then 40+/-10% of the magma in the lake crystallized. Based on RIMFAX data suggesting the Séítah formation was approximately 10m thick, this would lead to the bottom ~4m of the Séítah unit consisting of the Cine and Garde Bastide workspace olivine cumulate outcrop sampled by *Perseverance*. The original magma body would necessarily have been thicker to allow differentiation of the olivine crystals and settling to the bottom of the chamber. This upper part would be more pyroxene than

olivine-rich, as described in Wiens et al. (2022). It is likely that this portion of the magma lake was removed prior to emplacement of later lava flows.

6. As seen in Figure 6, there are regions of the CRISM HRL40FF image that display the presence of all three olivine, phyllosilicate, and carbonate bands (known as the marginal carbonates). However, there are regions where only phyllosilicates are present, with only a weak to vanishing 2.5  $\mu\text{m}$  band. This is marked “Phyllosilicate only” on the Figure 7 correlation plot.
7. As seen in Figure 4 and 10, the IR spectra of phyllosilicates talc, lizardite, Mg/Fe smectite, hectorite, saponite and stevensite, are broadly consistent with the spectra of Garde 207 and Dourbes Tailings 255. As seen in Figure 10, we have shown that talc is a strong match for the phyllosilicate signal in the VISIR spectra for Garde, and especially the Dourbes tailings. We regard the suggestion of talc to be only plausible or tentative until the VISIR calibration is further improved (Royer et al., this issue), or more observations are made in locations of higher phyllosilicate abundance, for example in the Marginal Carbonates region or potentially in the Noachian region outside of Jezero.
8. Based on the lack of a 2.28  $\mu\text{m}$  band, we can eliminate nontronite and hisingerite as the phyllosilicates in Gardes and Dourbes.
9. Based on Table 3, showing the LIBS results for Cine/Garde and Ubraye/Dourbes, the low aluminum amounts for the olivine cumulate are not consistent with the presence of Al bearing phyllosilicates.
10. We have formulated a new conjecture that the olivine-phyllosilicate-carbonate lithology is the missing earlier, more voluminous ultramafic rocks proposed by Rampey and Harvey (2012). Needless to say, this will require further testing in situ.

## 6. Acknowledgements

We would like to thank Paolo Pilleri, Chip Legett and Dot DeLapp for their untiring work to keep the SuperCam tools and datasets up to date and ready for use in projects like this one. We thank Daniel Applin for measurement of the stevensite spectra. We would also like to thank François Poulet, Janice Bishop, Deanne Rogers and an anonymous reviewer, for helpful comments and suggestions on the manuscript. We also thank all of the people who contributed to the development and operations of the *Perseverance* rover. This work is supported by grants and contracts to the Mars 2020 project as part of the Mars Exploration Program. AGF was supported by European Research Council, Consolidator Grant number

1133 818602.

1134

## 1135 Open Research

1136

1137 All CRISM and VISIR data used can be obtained from the Planetary Data System  
1138 (PDS) Geoscience Node (<http://ode.rsl.wustl.edu/mars>). All data and software used  
1139 to produce the datasets in this manuscript are available at the Harvard Dataverse  
1140 (<https://doi.org/10.7910/DVN/QEIVES>).

1141

1142

1143

## 1144 7. References

1145

1146

1147 Allwood, A.C., Wade, L.A., Foote, M.C., Elam, W.T., Hurowitz, J.A., Battel, S., Dawson, D.E.,  
1148 Denise, R.W., Ek, E.M., Gilbert, M.S., King, M.E., Liebe, C.C., Parker, T., Pedersen,  
1149 D.A.K., Randall, D.P., Sharrow, R.F., Sondheim, M.E., Allen, G., Arnett, K., Au, M.H.,  
1150 Basset, C., Benn, M., Bousman, J.C., Braun, D., Calvet, R.J., Clark, B., Cinquini, L.,  
1151 Conaby, S., Conley, H.A., Davidoff, S., Delaney, J., Denver, T., Diaz, E., Doran, G.B.,  
1152 Ervin, J., Evans, M., Flannery, D.O., Gao, N., Gross, J., Grotzinger, J., Hannah, B.,  
1153 Harris, J.T., Harris, C.M., He, Y., Heirwegh, C.M., Hernandez, C., Hertzberg, E., Hodyss,  
1154 R.P., Holden, J.R., Hummel, C., Jadusingh, M.A., Jørgensen, J.L., Kawamura, J.H.,  
1155 Kitiyakara, A., Kozaczek, K., Lambert, J.L., Lawson, P.R., Liu, Y., Luchik, T.S., Macneal,  
1156 K.M., Madsen, S.N., McLennan, S.M., McNally, P., Meras, P.L., Muller, R.E., Napoli, J.,  
1157 Naylor, B.J., Nemere, P., Ponomarev, I., Perez, R.M., Pootrakul, N., Romero, R.A.,  
1158 Rosas, R., Sachs, J., Schaefer, R.T., Schein, M.E., Setterfield, T.P., Singh, V., Song, E.,  
1159 Soria, M.M., Stek, P.C., Tallarida, N.R., Thompson, D.R., Tice, M.M., Timmermann, L.,  
1160 Torossian, V., Treiman, A., Tsai, S., Uckert, K., Villalvazo, J., Wang, M., Wilson, D.W.,  
1161 Worel, S.C., Zamani, P., Zappe, M., Zhong, F., Zimmerman, R., 2020. PIXL: Planetary  
1162 Instrument for X-Ray Lithochemistry. *Space Sci. Rev.* 216, 134.  
1163 <https://doi.org/10.1007/s11214-020-00767-7>

1164 Alwmark, S., 2022. Varied origins of Artuby signals complex series of geologic events in Jezero  
1165 crater, Mars. *J. Geophys. Res.* this volume.

1166 Amelin, Y., Krot, A.N., Hutcheon, I.D., Ulyanov, A.A., 2002. Lead Isotopic Ages of Chondrules  
1167 and Calcium-Aluminum-Rich Inclusions. *Science* 297, 1678–1683.

1168 <https://doi.org/10.1126/science.1073950>

1169 Anderson, R.B., Forni, O., Cousin, A., Wiens, R.C., Clegg, S.M., Frydenvang, J., Gabriel, T.S.J.,  
1170 Ollila, A., Schröder, S., Beyssac, O., Gibbons, E., Vogt, D.S., Clavé, E., Manrique, J.-A.,  
1171 Legett, C., Pilleri, P., Newell, R.T., Sarrao, J., Maurice, S., Arana, G., Benzerara, K.,  
1172 Bernardi, P., Bernard, S., Bousquet, B., Brown, A.J., Alvarez-Llamas, C., Chide, B.,  
1173 Cloutis, E., Comellas, J., Connell, S., Dehouck, E., Delapp, D.M., Essunfeld, A., Fabre,  
1174 C., Fouchet, T., Garcia-Florentino, C., García-Gómez, L., Gasda, P., Gasnault, O.,  
1175 Hausrath, E.M., Lanza, N.L., Laserna, J., Lasue, J., Lopez, G., Madariaga, J.M.,  
1176 Mandon, L., Mangold, N., Meslin, P.-Y., Nelson, A.E., Newsom, H., Reyes-Newell, A.L.,  
1177 Robinson, S., Rull, F., Sharma, S., Simon, J.I., Sobron, P., Fernandez, I.T., Udry, A.,  
1178 Venhaus, D., McLennan, S.M., Morris, R.V., Ehlmann, B., 2022. Post-landing major

- 1179 element quantification using SuperCam laser induced breakdown spectroscopy.  
 1180 Spectrochim. Acta Part B At. Spectrosc. 188, 106347.  
 1181 <https://doi.org/10.1016/j.sab.2021.106347>
- 1182 Arndt, N.T., Leshar, C.M., Houlé, M.G., Lewin, E., Lacaze, Y., 2004. Intrusion and crystallization  
 1183 of a spinifex-textured komatiite sill in Dundonald Township, Ontario. *J. Petrol.* 45, 2555–  
 1184 2571.
- 1185 Bailey, S.W., 1988. Hydrous phyllosilicates:(exclusive of micas). Walter de Gruyter GmbH & Co  
 1186 Bishop J. L., Noe Dobrea E. Z., McKeown N. K., Parente M., Ehlmann B. L., Michalski J. R.,  
 1187 Milliken R. E., Poulet F., Swayze G. A., Mustard J. F., Murchie S. L. & Bibring J.-P. 2008a  
 1188 Phyllosilicate diversity and past aqueous activity revealed at Mawrth Vallis, Mars.  
 1189 *Science*, **321**, 830-833.
- 1190 Bishop, J.L., Lane, M.D., Dyar, M.D., Brown, A.J., 2008b. Reflectance and emission  
 1191 spectroscopy of four groups of phyllosilicates: smectites, kaolinite-serpentines, chlorites  
 1192 and micas. *Clay Miner.* 43, 35–54.
- 1193 Bishop, J.L., Perry, K.A., Darby Dyar, M., Bristow, T.F., Blake, D.F., Brown, A.J., Peel, S.E.,  
 1194 2013. Coordinated spectral and XRD analyses of magnesite-nontronite-forsterite  
 1195 mixtures and implications for carbonates on Mars. *J. Geophys. Res. Planets* 635–650.
- 1196 Borg, L.E., Connelly, J.N., Nyquist, L.E., Shih, C.-Y., Wiesmann, H., Reese, Y., 1999. The age of  
 1197 the carbonates in Martian meteorite ALH84001. *Science* 286, 90–94.
- 1198 Bottinga, Y., Weill, D.F., 1972. The viscosity of magmatic silicate liquids: A model for calculation.  
 1199 *Am. J. Sci.* 272, 438–475.
- 1200 Brindley, G.W., Bish, D.L., Wan, H.-M., 1977. The nature of kerolite, its relation to talc and  
 1201 stevensite. *Mineral. Mag.* 41, 443–452.
- 1202 Brown, A. J., 2006. Spectral Curve Fitting for Automatic Hyperspectral Data Analysis. *IEEE*  
 1203 *Trans. Geosci. Remote Sens.* 44, 1601–1608.  
 1204 <https://doi.org/10.1109/TGRS.2006.870435>
- 1205 Brown, A.J., 2006. Hyperspectral Mapping of Ancient Hydrothermal Systems (PhD). Macquarie  
 1206 University, Sydney, N.S.W.
- 1207 Brown, Adrian, 2023, "Replication Data for: Properties of the Olivine-Clay-Carbonate lithology at  
 1208 Seitah", [Dataset] <https://doi.org/10.7910/DVN/QEIVES>, Harvard Dataverse, V3
- 1209 Brown, A.J., Hook, S.J., Baldrige, A.M., Crowley, J.K., Bridges, N.T., Thomson, B.J., Marion,  
 1210 G.M., de Souza Filho, C.R., Bishop, J.L., 2010. Hydrothermal formation of Clay-  
 1211 Carbonate alteration assemblages in the Nili Fossae region of Mars. *Earth Planet. Sci.*  
 1212 *Lett.* 297, 174–182. <https://doi.org/10.1016/j.epsl.2010.06.018>
- 1213 Brown, A.J., Viviano, C.E., Goudge, T.A., 2020. Olivine–Carbonate Mineralogy of the Jezero  
 1214 Crater Region. *J. Geophys. Res. Planets* 125, <https://doi.org/10.1029/2019JE006011>.
- 1215 Brown, A.J., Walter, M.R., Cudahy, T.J., 2005. Hyperspectral Imaging Spectroscopy of a Mars  
 1216 Analog Environment at the North Pole Dome, Pilbara Craton, Western Australia. *Aust. J.*  
 1217 *Earth Sci.* 52, 353–364. <https://doi.org/10.1080/08120090500134530>
- 1218

- 1219 Citron, R.I., Manga, M., Hemingway, D.J., 2018. Timing of oceans on Mars from shoreline  
1220 deformation. *Nature* 555, 643–646. <https://doi.org/10.1038/nature26144>
- 1221 Clark, R.N., Swayze, G.A., Wise, R., Livo, E., Hoefen, T., Kokaly, R., Sutley, S.J., 2007. USGS  
1222 digital spectral library splib06a: <http://speclab.cr.usgs.gov/spectral.lib06/>, Digital Data  
1223 Series 231. U.S. Geological Survey.
- 1224 Clave, E., et al., 2022. Carbonate detection with SuperCam in igneous rocks on the floor of  
1225 Jezero Crater, Mars. *J. Geophys. Res.* this volume.
- 1226 Corpolongo, A., et al., 2022. SHERLOC Raman mineral detections of the Mars 2020 Crater  
1227 Floor Campaign. *J. Geophys. Res.* this volume.
- 1228 Crumpler, L.S., et al., 2022. In Situ Geologic Context Mapping Transect on the Floor of Jezero  
1229 Crater from Mars 2020/Perseverance Rover Observations. *J. Geophys. Res.* this  
1230 volume.
- 1231 Duke, E.F., 1994. Near infrared spectra of muscovite, Tschermak substitution, and metamorphic  
1232 reaction progress: Implications for remote sensing. *Geology* 22, 621–624.
- 1233 Ehlmann, B.L., Mustard, J.F., Murchie, S.L., Poulet, F., Bishop, J.L., Brown, A.J., Calvin, W.M.,  
1234 Clark, R.N., Marais, D.J.D., Milliken, R.E., Roach, L.H., Roush, T.L., Swayze, G.A.,  
1235 Wray, J.J., 2008. Orbital Identification of Carbonate-Bearing Rocks on Mars. *Science*  
1236 322, 1828–1832. <https://doi.org/10.1126/science.1164759>
- 1237 Farley, K.A., Malespin, C., Mahaffy, P., Grotzinger, J.P., Vasconcelos, P.M., Milliken, R.E.,  
1238 Malin, M., Edgett, K.S., Pavlov, A.A., Hurowitz, J.A., Grant, J.A., Miller, H.B., Arvidson,  
1239 R., Beegle, L., Calef, F., Conrad, P.G., Dietrich, W.E., Eigenbrode, J., Gellert, R., Gupta,  
1240 S., Hamilton, V., Hassler, D.M., Lewis, K.W., McLennan, S.M., Ming, D., Navarro-  
1241 Gonz lez, R., Schwenzer, S.P., Steele, A., Stolper, E.M., Sumner, D.Y., Vaniman, D.,  
1242 Vasavada, A., Williford, K., Wimmer-Schweingruber, R.F., the, M.S.L.S.T., 2013. In Situ  
1243 Radiometric and Exposure Age Dating of the Martian Surface. *Science*.  
1244 <https://doi.org/10.1126/science.1247166>
- 1245
- 1246 Farley, K. A., K. M. Stack, D. L. Shuster, B. H. N. Horgan, J. A. Hurowitz, J. D. Tarnas, J. I.  
1247 Simon, et al. “Aqueously Altered Igneous Rocks Sampled on the Floor of Jezero Crater,  
1248 Mars.” *Science* 377, no. 6614 (August 25, 2022): eabo2196.  
1249 <https://doi.org/10.1126/science.abo2196>.
- 1250 Farley, K.A., Williford, K.H., Stack, K.M., Bhartia, R., Chen, A., de la Torre, M., Hand, K.,  
1251 Goreva, Y., Herd, C.D.K., Hueso, R., Liu, Y., Maki, J.N., Martinez, G., Moeller, R.C.,  
1252 Nelessen, A., Newman, C.E., Nunes, D., Ponce, A., Spanovich, N., Willis, P.A., Beegle,  
1253 L.W., Bell, J.F., Brown, A.J., Hamran, S.-E., Hurowitz, J.A., Maurice, S., Paige, D.A.,  
1254 Rodriguez-Manfredi, J.A., Schulte, M., Wiens, R.C., 2020. Mars 2020 Mission Overview.  
1255 *Space Sci. Rev.* 216, 142. <https://doi.org/10.1007/s11214-020-00762-y>
- 1256 Garc a-Romero, E., Lorenzo, A., Garc a-Vicente, A., Morales, J., Garc a-Rivas, J., Su rez, M.,  
1257 2021. On the structural formula of smectites: a review and new data on the influence of  
1258 exchangeable cations. *J. Appl. Crystallogr.* 54, 251–262.  
1259 <https://doi.org/10.1107/S1600576720016040>
- 1260 Goudge, T.A., Mohrig, D., Cardenas, B.T., Hughes, C.M., Fassett, C.I., 2018. Stratigraphy and  
1261 paleohydrology of delta channel deposits, Jezero crater, Mars. *Icarus* 301, 58–75.
- 1262 Goudge, T.A., Mustard, J.F., Head, J.W., Fassett, C.I., Wiseman, S.M., 2015. Assessing the  
1263 Mineralogy of the Watershed and Fan Deposits of the Jezero Crater Paleolake System,  
1264 Mars. *J. Geophys. Res. Planets* 2014JE004782. <https://doi.org/10.1002/2014JE004782>
- 1265 Grosch, Eugene G., Janice L. Bishop, Christian Mielke, Alessandro Maturilli, and J rn Helbert.  
1266 “Early Archean Alteration Minerals in Mafic-Ultramafic Rocks of the Barberton  
1267 Greenstone Belt as Petrological Analogs for Clay Mineralogy on Mars.” *American*



- Mineralogist 106, no. 5 (May 1, 2021): 672–84. <https://doi.org/10.2138/am-2021-7656>.
- Guest, J. E., C. R. J. Kilburn, H. Pinkerton, and A. M. Duncan. “The Evolution of Lava Flow-Fields: Observations of the 1981 and 1983 Eruptions of Mount Etna, Sicily.” *Bulletin of Volcanology* 49, no. 3 (June 1, 1987): 527–40. <https://doi.org/10.1007/BF01080447>.
- Hamilton, V.E., Christensen, P.R., 2005. Evidence for extensive, olivine-rich bedrock on Mars. *Geology* 33, 433–436.
- Hamran, Svein-Erik, David A. Paige, Abigail Allwood, Hans E. F. Amundsen, Tor Berger, Sverre Brovoll, Lynn Carter, et al. “Ground Penetrating Radar Observations of Subsurface Structures in the Floor of Jezero Crater, Mars.” *Science Advances* 8, no. 34 (August 26, 2022): eabp8564. <https://doi.org/10.1126/sciadv.abp8564>.
- Hiesinger, H., Head, J.W., 2004. The Syrtis Major volcanic province, Mars: Synthesis from Mars Global Surveyor data. *J. Geophys. Res.* 109, 10.1029/2003JE002143.
- Hoefen, T.M., Clark, R.N., Bandfield, J.L., Smith, M.D., Pearl, J.C., Christensen, P.R., 2003. Discovery of Olivine in the Nili Fossae Region of Mars. *Science* 302, 627–630.
- Horgan, B.H.N., Anderson, R.B., Dromart, G., Amador, E.S., Rice, M.S., 2020. The mineral diversity of Jezero crater: Evidence for possible lacustrine carbonates on Mars. *Icarus* 113526. <https://doi.org/10.1016/j.icarus.2019.113526>
- Huppert, H.E., Sparks, R.S.J., 1985. Cooling and contamination of mafic and ultramafic magmas during ascent through continental crust. *Earth Planet. Sci. Lett.* 74, 371–386.
- Huppert, H.E., Sparks, R.S.J., 1981. The fluid dynamics of a basaltic magma chamber replenished by influx of hot, dense ultrabasic magma. *Contrib. Mineral. Petrol.* 75, 279–289. <https://doi.org/10.1007/BF01166768>
- Huppert, H.E., Sparks, R.S.J., Turner, J.S., Arndt, N.T., 1984. Emplacement and cooling of komatiite lavas. *Nature* 309, 13–16.
- Isherwood, R.J., Jozwiak, L.M., Jansen, J.C., Andrews-Hanna, J.C., 2013. The volcanic history of Olympus Mons from paleo-topography and flexural modeling. *Earth Planet. Sci. Lett.* 363, 88–96.
- Itoh Y. & Parente M. (2021) A new method for atmospheric correction and de-noising of CRISM hyperspectral data. *Icarus*, 354, 114024.
- Kremer, C.H., Mustard, J.F., Bramble, M.S., 2019. A widespread olivine-rich ash deposit on Mars. *Geology*. <https://doi.org/10.1130/G45563.1>
- Lapen, T.J., Righter, M., Brandon, A.D., Debaille, V., Beard, B.L., Shafer, J.T., Peslier, A.H., 2010. A Younger Age for ALH84001 and Its Geochemical Link to Shergottite Sources in Mars. *Science* 328, 347–351.
- Liu, Y., M. M. Tice, M. E. Schmidt, A. H. Treiman, T. V. Kizovski, J. A. Hurowitz, A. C. Allwood, et al. “An Olivine Cumulate Outcrop on the Floor of Jezero Crater, Mars.” *Science* 377, no. 6614 (September 30, 2022): 1513–19. <https://doi.org/10.1126/science.abo2756>.
- Mandon, L., et al., 2022. Reflectance of Jezero crater floor: 2. Mineralogical interpretation. *J. Geophys. Res.* this volume.
- Mandon, L., Beck, P., Quantin-Nataf, C., Dehouck, E., Thollot, P., Loizeau, D., Volat, M., 2022. ROMA: A Database of Rock Reflectance Spectra for Martian In Situ Exploration. *Earth Space Sci.* 9, e2021EA001871. <https://doi.org/10.1029/2021EA001871>
- Mandon, L., Quantin-Nataf, C., Thollot, P., Mangold, N., Lozac’h, L., Dromart, G., Beck, P., Dehouck, E., Breton, S., Millot, C., Volat, M., 2020. Refining the age, emplacement and alteration scenarios of the olivine-rich unit in the Nili Fossae region, Mars. *Icarus* 336, 113436. <https://doi.org/10.1016/j.icarus.2019.113436>
- Mangold, N., Gupta, S., Gasnault, O., Dromart, G., Tarnas, J.D., Sholes, S.F., Horgan, B., Quantin-Nataf, C., Brown, A.J., Le Mouélic, S., 2021. Perseverance rover reveals an ancient delta-lake system and flood deposits at Jezero crater, Mars. *Science* eabl4051.

- Mangold, N., D. Loizeau, F. Poulet, V. Ansan, D. Baratoux, S. LeMouelic, J. M. Bardintzeff, et al. "Mineralogy of Recent Volcanic Plains in the Tharsis Region, Mars, and Implications for Platy-Ridged Flow Composition." *Earth and Planetary Science Letters*, Mars Express after 6 Years in Orbit: Mars Geology from Three-Dimensional Mapping by the High Resolution Stereo Camera (HRSC) Experiment, 294, no. 3 (June 1, 2010): 440–50. <https://doi.org/10.1016/j.epsl.2009.07.036>.
- Mangold, N., Poulet, F., Mustard, J.F., Bibring, J.P., Gondet, B., Langevin, Y., Ansan, V., Masson, P., Fassett, C., Head, J.W., III, Hoffmann, H., Neukum, G., 2007. Mineralogy of the Nili Fossae region with OMEGA/Mars Express data: 2. Aqueous alteration of the crust. *J. Geophys. Res.* 112, doi:10.1029/2006JE002835.
- Martin, P.E., Farley, K.A., Baker, M.B., Malespin, C.A., Schwenzer, S.P., Cohen, B.A., Mahaffy, P.R., McAdam, A.C., Ming, D.W., Vasconcelos, P.M., Navarro-González, R., 2017. A Two-Step K-Ar Experiment on Mars: Dating the Diagenetic Formation of Jarosite from Amazonian Groundwaters. *J. Geophys. Res. Planets* 122, 2803–2818. <https://doi.org/10.1002/2017JE005445>
- Maurice, S., Wiens, R.C., Bernardi, P., Caïs, P., Robinson, S., Nelson, T., Gasnault, O., Reess, J.-M., Deleuze, M., Rull, F., 2021. The SuperCam instrument suite on the Mars 2020 rover: Science objectives and Mast-Unit description. *Space Sci. Rev.* 217, 1–108.
- Mustard, J.F., Poulet, F., Head, J.W., Mangold, N., Bibring, J.P., Pelkey, S.M., Fassett, C.I., Langevin, Y., Neukum, G., 2007. Mineralogy of the Nili Fossae region with OMEGA/Mars Express data: 1. Ancient impact melt in the Isidis Basin and implications for the transition from the Noachian to Hesperian. *J. Geophys. Res.* 112.
- Núñez, J., et al., 2022. Stratigraphy and Mineralogy of the Séítah formation on the floor of Jezero crater, Mars, as seen with Mastcam-Z. *J. Geophys. Res.* this volume.
- Nyquist, L.E., Shih, C.-Y., McCubbin, F.M., Santos, A.R., Shearer, C.K., Peng, Z.X., Burger, P.V., Agee, C.B., 2016. Rb-Sr and Sm-Nd isotopic and REE studies of igneous components in the bulk matrix domain of Martian breccia Northwest Africa 7034. *Meteorit. Planet. Sci.* 51, 483–498. <https://doi.org/10.1111/maps.12606>
- Pinet, P., Chevrel, S., 1990. Spectral Identification of Geological Units on the Surface of Mars Related to the Presence of Silicates From Earth-Based Near-Infrared Telescopic Charge-Coupled Device Imaging. *J. Geophys. Res.* 95, 14435.
- Parente, Mario, Arun M. Saranathan, Yuki Itoh, Jesse D. Tarnas, Frank P. Seelos, and John F. Mustard. "Map of the Dominant Mineralogy over and around the Mars2020 Landing Ellipse with Correspondent Spectral Signatures," October 14, 2021. <https://doi.org/10.5281/zenodo.5575824>.
- Pinkerton, H., Wilson, L., 1994. Factors controlling the lengths of channel-fed lava flows. *Bull. Volcanol.* 56, 108–120. <https://doi.org/10.1007/BF00304106>
- Plescia, J.B., 1990. Recent flood lavas in the Elysium region of Mars. *Icarus* 88, 465–490.
- Putirka, K., 2016. Rates and styles of planetary cooling on Earth, Moon, Mars, and Vesta, using new models for oxygen fugacity, ferric-ferrous ratios, olivine-liquid Fe-Mg exchange, and mantle potential temperature. *Am. Mineral.* 101, 819–840. <https://doi.org/10.2138/am-2016-5402>
- Rampey, M., Harvey, R., 2012. Mars Hesperian Magmatism as Revealed by Syrtis Major and the Circum-Hellas Volcanic Province. *Earth Moon Planets* 109, 61–75. <https://doi.org/10.1007/s11038-012-9404-0>
- Ravanis, E., Fagents, S.A., Newman, C.E., Horgan, B.H., Holm-Alwmark, S., Brown, A.J., Rice Jr, J.W., Mandon, L., Zorzano, M.-P., 2022. The Potential for Pyroclastic Deposits in the Jezero Crater Region of Mars from Ash Dispersal Modeling, in: LPSC. Presented at the

- 1370 53rd Lunar and Planetary Science Conference, LPI, Houston, TX, p. Abstract #1692.
- 1371 Robbins, S.J., Achille, G.D., Hynek, B.M., 2011. The volcanic history of Mars: High-resolution
- 1372 crater-based studies of the calderas of 20 volcanoes. *Icarus* 211, 1179–1203.
- 1373 <https://doi.org/10.1016/j.icarus.2010.11.012>
- 1374 Rogers, D., Warner Nicholas H., Golombek Matthew P., Head James W., Cowart Justin C.,
- 1375 2018. Areal Extensive Surface Bedrock Exposures on Mars: Many Are Clastic Rocks,
- 1376 Not Lavas. *Geophys. Res. Lett.* 45, 1767–1777. <https://doi.org/10.1002/2018GL077030>
- 1377 Roush, T.L., Bishop, J.L., Brown, A.J., Blake, D.F., Bristow, T.F., 2015. Laboratory reflectance
- 1378 spectra of clay minerals mixed with Mars analog materials: Toward enabling quantitative
- 1379 clay abundances from Mars spectra. *Icarus* 258, 454–466.
- 1380 <https://doi.org/10.1016/j.icarus.2015.06.035>
- 1381 Royer, C., et al., 2022. Reflectance of Jezero crater floor: 1. Data processing and calibration of
- 1382 IRS/SuperCam. *J. Geophys. Res.* this volume.
- 1383 Ruff, S.W., Hamilton, V.E., Rogers, A.D., Edwards, C.S., Horgan, B.H.N., 2022. Olivine and
- 1384 carbonate-rich bedrock in Gusev crater and the Nili Fossae region of Mars may be
- 1385 altered ignimbrite deposits. *Icarus* 380, 114974.
- 1386 <https://doi.org/10.1016/j.icarus.2022.114974>
- 1387 Saranthan, A.M. and Parente, M (2021) Adversarial feature learning for improved mineral
- 1388 mapping of CRISM data. *Icarus* 355 114107
- 1389 Seelos, F. P., M. F. Morgan, H. W. Taylor, S. L. Murchie, D. C. Humm, K. D. Seelos, O.
- 1390 S. Barnouin, C. E. Viviano, and CRISM Team (2012), CRISM Map Projected
- 1391 Targeted Reduced Data Records (MTRDRs) – High Level Analysis and
- 1392 Visualization Data Products, in *Planetary Data: A Workshop for Users and*
- 1393 *Software Developers*, Flagstaff, AZ
- 1394 Spera, Frank J. “Aspects of Magma Transport.” Edited by R. B. Hargraves. *Physics of*
- 1395 *Magmatic Processes* 7 (1980).
- 1396 Sparks, R. S. J., H. Pinkerton, and R. Macdonald. “The Transport of Xenoliths in
- 1397 Magmas.” *Earth and Planetary Science Letters* 35, no. 2 (June 1, 1977): 234–38.
- 1398 [https://doi.org/10.1016/0012-821X\(77\)90126-1](https://doi.org/10.1016/0012-821X(77)90126-1).
- 1399 Shahrzad, S., Kinch, K.M., Goudge, T.A., Fassett, C.I., Needham, D.H., Quantin-Nataf, C.,
- 1400 Knudsen, C.P., 2019. Crater statistics on the dark-toned, mafic floor unit in Jezero
- 1401 Crater, Mars. *Geophys. Res. Lett.* 0. <https://doi.org/10.1029/2018GL081402>
- 1402 Sholes, S.F., Dickeson, Z.I., Montgomery, D.R., Catling, D.C., 2021. Where are Mars’
- 1403 hypothesized ocean shorelines? Large lateral and topographic offsets between different
- 1404 versions of paleoshoreline maps. *J. Geophys. Res. Planets* 126, e2020JE006486.
- 1405 Sholes, S.F., Rivera-Hernández, F., 2022. Constraints on the uncertainty, timing, and magnitude
- 1406 of potential Mars oceans from topographic deformation models. *Icarus* 378, 114934.
- 1407 Simon, J.I., et al., 2022. Samples Collected from the Floor of Jezero Crater with the Mars 2020
- 1408 Perseverance Rover. *J. Geophys. Res.* this volume.
- 1409 Stack, K.M., Williams, N.R., Calef, F., Sun, V.Z., Williford, K.H., Farley, K.A., Eide, S., Flannery,
- 1410 D., Hughes, C., Jacob, S.R., Kah, L.C., Meyen, F., Molina, A., Nataf, C.Q., Rice, M.,
- 1411 Russell, P., Scheller, E., Seeger, C.H., Abbey, W.J., Adler, J.B., Amundsen, H., Anderson,
- 1412 R.B., Angel, S.M., Arana, G., Atkins, J., Barrington, M., Berger, T., Borden, R., Boring, B.,
- 1413 Brown, A., Carrier, B.L., Conrad, P., Dypvik, H., Fagents, S.A., Gallegos, Z.E.,
- 1414 Garczynski, B., Golder, K., Gomez, F., Goreva, Y., Gupta, S., Hamran, S.-E., Hicks, T.,
- 1415 Hinterman, E.D., Horgan, B.N., Hurowitz, J., Johnson, J.R., Lasue, J., Kronyak, R.E.,
- 1416 Liu, Y., Madariaga, J.M., Mangold, N., McClean, J., Miklusicak, N., Nunes, D., Rojas, C.,
- 1417 Runyon, K., Schmitz, N., Scudder, N., Shaver, E., SooHoo, J., Spaulding, R., Stanish,
- 1418 E., Tamppari, L.K., Tice, M.M., Turenne, N., Willis, P.A., Aileen Yingst, R., 2020.
- 1419 Photogeologic Map of the Perseverance Rover Field Site in Jezero Crater Constructed

- 1420 by the Mars 2020 Science Team. *Space Sci. Rev.* 216, 127.  
 1421 <https://doi.org/10.1007/s11214-020-00739-x>
- 1422 Sun, V.Z., et al., 2022. Exploring the Jezero Crater Floor: Summary and Synthesis of  
 1423 Perseverance's First Science Campaign. *J. Geophys. Res.* this volume.
- 1424 Tarnas, J.D., Stack, K.M., Parente, M., Koepfel, A.H.D., Mustard, J.F., Moore, K.R., Horgan,  
 1425 B.H.N., Seelos, F.P., Cloutis, E.A., Kelemen, P.B., Flannery, D., Brown, A.J., Frizzell,  
 1426 K.R., Pinet, P., 2021. Characteristics, Origins, and Biosignature Preservation Potential of  
 1427 Carbonate-Bearing Rocks Within and Outside of Jezero Crater. *J. Geophys. Res.*  
 1428 *Planets* 126, e2021JE006898. <https://doi.org/10.1029/2021JE006898>
- 1429 Tice, M.M., et al., 2022. Primary and Alteration Textures of Séítah Formation Rocks Inferred by  
 1430 X-ray Fluorescence and Diffraction. *Sci. Adv.*
- 1431 Tornabene, L.L., Moersch, J.E., McSween, H.Y., Hamilton, V.E., Piatek, J.L., Christensen, P.R.,  
 1432 2008. Surface and crater-exposed lithologic units of the Isidis Basin as mapped by  
 1433 coanalysis of THEMIS and TES derived data products. *J. Geophys. Res. Planets* 113,  
 1434 E10001. <https://doi.org/10.1029/2007JE002988>
- 1435 Treiman, A.H., 2005. The nakhlite meteorites: Augite-rich igneous rocks from Mars.  
 1436 *Geochemistry* 65, 203–270. <https://doi.org/10.1016/j.chemer.2005.01.004>
- 1437 Treiman, A.H., Morris, R.V., Agresti, D.G., Graff, T.G., Achilles, C.N., Rampe, E.B., Bristow, T.F.,  
 1438 Ming, D.W., Blake, D.F., Vaniman, D.T., Bish, D.L., Chipera, S.J., Morrison, S.M., Downs,  
 1439 R.T., 2014. Ferrian saponite from the Santa Monica Mountains (California, U.S.A.,  
 1440 Earth): Characterization as an analog for clay minerals on Mars with application to  
 1441 Yellowknife Bay in Gale Crater. *Am. Mineral.* 99, 2234–2250. [https://doi.org/10.2138/am-](https://doi.org/10.2138/am-2014-4763)  
 1442 [2014-4763](https://doi.org/10.2138/am-2014-4763)
- 1443 Turrenne, N., Sidhu, S., Applin, D.M., Cloutis, E.A., Mertzman, S.A., Hausrath, E.M., 2023.  
 1444 Spectral properties of Nontronite under Earth surface conditions, Mars-like surface  
 1445 conditions, and (impact) heating events: Implications for instrument detections on Mars.  
 1446 *Icarus*.
- 1447 Udry, A., et al., 2022. A Mars2020 Perseverance SuperCam Perspective on the Igneous Nature  
 1448 of the Maaz formation at Jezero crater and link with Seitah, Mars. *J. Geophys. Res.* this  
 1449 volume.
- 1450 Van Kranendonk, M. J., Hickman, A. H., Smithies, R. H., Nelson, D. R. and Pike, G.  
 1451 (2002) Geology and tectonic evolution of the archean North Pilbara terrain, Pilbara  
 1452 Craton, Western Australia. *Economic Geology and the Bulletin of the Society of*  
 1453 *Economic Geologists*, 97 (4), 695-732.
- 1454
- 1455
- 1456 Vaucher, J., D. Baratoux, M. J. Toplis, P. Pinet, N. Mangold, and K. Kurita. "The Morphologies of  
 1457 Volcanic Landforms at Central Elysium Planitia: Evidence for Recent and Fluid Lavas on  
 1458 Mars." *Icarus* 200, no. 1 (March 1, 2009): 39–51.  
 1459 <https://doi.org/10.1016/j.icarus.2008.11.005>.
- 1460 Werner, S.C., 2008. The early martian evolution—Constraints from basin formation ages. *Icarus*  
 1461 195, 45–60. <https://doi.org/10.1016/j.icarus.2007.12.008>
- 1462 Wichman, R.W., Schultz, P.H., 1989. Sequence and mechanisms of deformation around the  
 1463 Hellas and Isidis Impact Basins on Mars. *J. Geophys. Res. Solid Earth* 94, 17333–  
 1464 17357. <https://doi.org/10.1029/JB094iB12p17333>
- 1465 Wiens, R.C., et al., 2022. Compositionally Stratified terrain in Jezero Crater. *Sci. Adv.*
- 1466 Wiens, R.C., Maurice, S., Robinson, S.H., Nelson, A.E., Cais, P., Bernardi, P., Newell, R.T.,  
 1467 Clegg, S., Sharma, S.K., Storms, S., 2021. The SuperCam instrument suite on the

- 1468 NASA Mars 2020 rover: Body unit and combined system tests. *Space Sci. Rev.* 217, 1–  
 1469 87.
- 1470 Williford, K.H., Farley, K.A., Stack, K.M., Allwood, A.C., Beaty, D., Beegle, L.W., Bhartia, R.,  
 1471 Brown, A.J., de la Torre Juarez, M., Hamran, S.-E., Hecht, M.H., Hurowitz, J.A.,  
 1472 Rodriguez-Manfredi, J.A., Maurice, S., Milkovich, S., Wiens, R.C., 2018. Chapter 11 -  
 1473 The NASA Mars 2020 Rover Mission and the Search for Extraterrestrial Life, in: Cabrol,  
 1474 N.A., Grin, E.A. (Eds.), *From Habitability to Life on Mars*. Elsevier, pp. 275–308.  
 1475 <https://doi.org/10.1016/B978-0-12-809935-3.00010-4>
- 1476 Wilson, L., Head, J.W., 1994. Mars - Review and Analysis of Volcanic-Eruption Theory and  
 1477 Relationships to Observed Landforms. *Rev. Geophys.* 32, 221–263.
- 1478 Worster, M.G., Huppert, H.E., Sparks, R.S.J., 1993. The crystallization of lava lakes. *J.*  
 1479 *Geophys. Res. Solid Earth* 98, 15891–15901. <https://doi.org/10.1029/93JB01428>
- 1480 Zastrow, A.M., Glotch, T.D., 2021. Distinct carbonate lithologies in Jezero crater, Mars.  
 1481 *Geophys. Res. Lett.* 48, e2020GL092365.
- 1482